Sodium MRI of Healthy Human Skin

by

Jingxuan Zhu

A thesis submitted in partial fulfillment of the requirements for the degree of

Master of Science

Department of Biomedical Engineering

University of Alberta

Abstract

Measuring skin sodium content has attracted significant interest due to its potential as a biomarker for various diseases, including dermatological conditions, cardiovascular disease, kidney disease, and diabetes. Skin sodium content can also vary between males and females and increases with age in healthy individuals. Non-invasive quantification of skin tissue sodium concentration (TSC) in vivo using sodium magnetic resonance imaging (MRI) could provide valuable insights for monitoring disease progression and understanding sodium regulation in the body. Various studies have quantified human skin TSC using MRI. A commonly adopted method, first proposed in 2012 by Kopp et al, uses a volume coil, GRE sequence with TE=2 ms, and 3×3×30 mm^3 voxels and has been widely adopted in skin sodium MRI studies. This method has limitations: TE=2 ms causes significant signal loss due to the rapid biexponential signal decay of sodium in the skin, and the large voxel size leads to partial volume effects because the skin is only 1-2 mm thick, affecting TSC quantification accuracy. This thesis aims to address these limitations by reducing signal loss and improving the accuracy of skin TSC measurements in healthy human skin using a surface coil and twisted-projection imaging (TPI) with smaller, reshaped voxels.

Sodium images of calf skin were acquired on a 4.7T MRI scanner from 14 healthy adults using TPI with a short echo time (TE) of approximately 0.1 ms. Initially, images were captured with a volume radiofrequency (RF) coil using voxels measuring 1.5×1.5×15 mm^3 (^{23}Na MRI protocol denoted here as *VolPencil*), following the widely adopted skin imaging protocol. Subsequently, a 5 cm diameter surface RF coil was employed, allowing

for five times smaller voxels (0.8×0.8×10 mm³) while maintaining a similar signal-to-noise ratio (SNR) within the same 12-minute scan time (*SurfPencil*). These 'pencil-shaped' voxels were replaced with 'pancake-shaped' voxels (0.4×4×4 =6.4 mm³), better matching the anatomy of pressed flat skin (*SurfPancake*). The B_1 field of the surface coil was investigated using a novel spin-3/2 simulation. The relationship between TSC measurement and skin thickness was also investigated.

Results indicated that the higher resolution *SurfPencil* approach yielded a 44±16% greater skin sodium image intensity compared to *VolPencil*, while *SurfPancake* provided an additional 20±9% increase ($p < 1e-8$), indicating reduced signal loss. Across participants with skin thicknesses ranging from 1.0 to 1.8 mm, sodium intensity significantly increased by 56%±19% and 44%±12% as a function of greater skin thickness for *VolPencil* and *SurfPencil*, respectively ($p < 0.003$), but not for *SurfPancake*, indicating reduced bias when pancake-shaped voxels are used. Imaging with *SurfPancake* measured a skin sodium concentration of 34±5 mM, greater than the ~20 mM measured using the widely adopted protocol but still much lower than the 85 mM measured by atomic absorption spectroscopy. Simulation, which matched experimental trends, identified a remaining 64% signal loss from signal loss during RF pulse and point spread function (PSF) smearing. Relaxation-based compensation yielded a concentration of 95±15 mM, similar to the value obtained by atomic absorption spectroscopy.

These findings suggest that previously published studies using volume RF coils with suboptimal spatial resolution may have underestimated skin sodium content due to partial

volume effects from adjacent tissues like adipose, muscle and air. Consequently, observed sex differences or disparities between healthy and diseased states in earlier studies could be partially attributed to varying skin thickness rather than true physiological differences.

By adopting TPI sequence with 0.1 ms TE, surface coil and 6.4 mm^3 voxels with only 0.4 mm voxel dimensions across the skin, these errors have been mitigated, providing more accurate measurements of skin sodium concentration. Further, relaxation-based signal compensation demonstrated that it is feasible to compensate for signal loss with T_2 relaxation parameters, suggesting a future direction of measuring individual relaxation values for more accurate skin TSC estimation. It is important to acknowledge the limitations of this approach, as measurements are confined to a small region of skin, and the entire cross-section of the leg is not imaged. Despite these limitations, this study offers a promising tool for overcoming challenges in sodium quantification and could lead to more precise assessments of sodium regulation and disease progression in the human body.

Preface

This thesis is an original work by Jingxuan Zhu. The research project, of which this thesis is part, was funded by the Natural Sciences and Engineering Research Council of Canada (NSERC).

All volunteer subjects were scanned at the Peter S. Allen MRI Research Center at the University of Alberta Hospital and written informed consent was obtained.

A version of Chapter 3 of this thesis has been submitted for publication.

Acknowledgments

I would like to express my deepest gratitude to those who have supported me throughout the journey of this degree program.

First and foremost, I am profoundly thankful to my advisor, Dr. Christian Beaulieu, for your invaluable guidance, constant encouragement, and insightful feedback. Your expertise and dedication have greatly enriched my academic journey.

I extend my sincere appreciation to Dr. Rob Stobbe, for your expertise, mentorship, guidance, and support throughout the completion of this project and my degree. I also want to thank Karim Damji for building the hardware for this study and helping me numerous times with conducting experiments.

I am also extremely grateful to my colleagues and friends who became my chosen family overseas—you know who you are. I wish you all the best in your future academic endeavors and in every aspect of your lives. Also to my friends back home—you are truly important to me and it won't be long till we meet again.

A special thanks goes to my boyfriend, Zhaoxiang Zhang, for your unconditional love and support, and to my favorite furry buddy, Mocha, for brightening up each and every day of my life!

Table of Contents

List of Tables

List of Figures

Symbols and Abbreviations

2D	Two dimensional
3D	Three dimensional
3DPR	3D projection reconstruction
ATP	Adenosine Triphosphate
ADP	Adenosine Diphosphate
B_0	Static Magnetic Field
B_1	Radiofrequency Magnetic Field
B_1^+	Transmit Radiofrequency Field
B_1^-	Reception Radiofrequency Field
BMI	Body Mass Index
BLOSI	Bloch-Siegert off-resonance Method
COX-2	Cyclooxygenase-2
CVD	Cardiovascular Disease
CKD	Chronic Kidney Disease
DAM	Double-Angle Method
DQF	Double quantum filtering
ECF	Extracellular Fluid
ESL	Endothelial Surface Layer
FA	Flip Angle
FLORET	Fermat looped, orthogonally encoded trajectories
FOV	Field of View
GAG	Glycosaminoglycan
GRE	Gradient Echo

HD	Hemodialysis
I	Spin Quantum Number
M_0	Net Magnetization
MHD	PD and Maintenance Hemodialysis
MRI	Magnetic Resonance Imaging
M_{xy}	Transverse Magnetization
M_z	Longitudinal Magnetization
NMR	Nuclear Magnetic Resonance
PAI	Primary Adrenal Insufficiency
PGE2	Prostaglandin E2
PHA	Primary Hyperaldosteronism
PSF	Point Spread Function
Q	Quality Factor
Q_{loaded}	Loaded Quality Factor
$Q_{unloaded}$	Unloaded Quality Factor
RAAS	Renin-Angiotensin-Aldosterone System
rB_1^+	Relative Transmit RF Field
RF	Radiofrequency
ROI	Region of Interest
SI	Signal Intensity
SLE	Systemic Lupus Erythematosus
SNR	Signal-to-Noise Ratio
SSc	Systemic Sclerosis
TE	Echo time
TH2	T-helper

TH17	T-helper 17
T_1	Longitudinal Relaxation Time
T_2	Transverse Relaxation Time
T_2^*	Apparent Transverse Relaxation Time
T2DM	Type 2 Diabetes Mellitus
T_{2fast}	Fast component of T_2
T_{2slow}	Slow component of T_2
TPI	Twisted Projection Imaging
TQF	Triple Quantum filtering
TR	Repetition Time
TSC	Tissue Sodium Concentration
UTE	Ultrashort Echo Time
VEGF-C	Vascular Endothelial Growth Factor-C
ω_0	Larmor Frequency
ω_Q	Quadrupole Frequency
γ	Gyromagnetic Ratio
μ	Magnetic Moment

1. Introduction

1.1 Thesis Introduction

Sodium MRI in the skin has been an area of growing interest. While the skin is hypothesized to play an important role in regulating sodium content in the body, acting as a buffer for excessive amounts of sodium, this remains a subject of ongoing research and is not yet definitively established[1]. Sodium ions are strongly associated ('bind') with negatively charged glycosaminoglycans (GAGs) in the extracellular matrix of the skin[2–4], contributing to the skin's role in maintaining sodium balance and influencing blood pressure[1]. Research has demonstrated that skin sodium content may be elevated in various pathological conditions (to be discussed later). Moreover, it may also increase with age[5–7] and differ between males and females[5,8]. However, these findings remain subject to further investigation, and the current body of research should be interpreted with caution.

Non-invasive techniques, such as sodium MRI, could monitor skin sodium content, providing valuable insights into an individual's sodium balance and aiding in the diagnosis and management of conditions like hypertension[5] and chronic kidney disease[9]. Exploring interactions between sodium storage in the skin and other physiological systems could lead to targeted treatments. For example, therapies aimed at modifying the skin's sodium storage capacity or enhancing the mobilization of stored sodium might benefit patients with cardiovascular and renal diseases[10].

Quantifying sodium content in the skin presents several challenges. One of the primary difficulties is the relatively low concentration of sodium ions compared to the proton density in the skin, resulting in a weak MRI signal. This low sodium signal inherently limits the amount of collectible data. Furthermore, the biexponential T_2 relaxation time for sodium in biological tissues is significantly shorter than that of protons. To mitigate this rapid signal decay, it is necessary to use short echo times (TE) in order to capture a greater amount of signal. Sodium MRI typically requires larger voxels to achieve adequate signal-to-noise ratio (SNR), which, combined with the thin anatomy of the skin, increases the effect of partial volume averaging.

Previous studies, such as those conducted by Kopp et al[5,8,11,12], have utilized low SNR radiofrequency (RF) volume coils, resulting in the need for larger voxel sizes. Plus, the standard gradient-recalled echo (GRE) sequence was implemented in most existing skin sodium MRI studies, which resulted in longer echo times, further reducing SNR. Volume coils, while beneficial for their uniformity in signal reception, often lack the sensitivity required for detecting low concentrations of sodium in small tissue volumes, such as skin.

To address these challenges, this thesis aims to minimize signal loss and enhance the accuracy of skin tissue sodium concentration (TSC) measurements by using a more sensitive surface RF coil. Volume coils will still be used to maintain consistency with previous studies, while the surface coil is employed to facilitate the use of smaller voxels. Surface coils provide higher SNR for regions proximal to the coil, making them particularly suitable for skin imaging.

Additionally, this approach incorporates using a twisted projection imaging (TPI) sequence with a short TE to more effectively capture the rapidly decaying sodium signal. Various flip angles (60°, 90°, and 120°) are prescribed for B_1 mapping to correct signal intensity. This combination of techniques is expected to significantly improve the resolution and accuracy of sodium imaging in the skin, providing more reliable data for future research.

Sodium MRI offers significant potential for non-invasive quantification of skin sodium content, enhancing our understanding of physiological and pathological conditions. By overcoming challenges related to low sodium concentration and rapid signal decay through optimized imaging parameters and techniques, the accuracy and reliability of sodium MRI can be improved. This advancement could aid in elucidating the skin's role in sodium regulation and its disease implications.

1.2 Sodium Physiology in Skin

1.2.1 Sodium Function and Sodium Regulation in the Human Body

Sodium is an important electrolyte in the human body that plays a vital role in many physiological functions. It is essential for transmitting nerve impulses by facilitating the propagation of action potentials along neurons, which is crucial for communication between the brain and the rest of the body[13,14]. Furthermore, sodium regulates blood pressure by attracting and retaining water in the blood vessels, thereby sustaining blood volume and contributing to overall blood pressure[15].

In addition to these roles, sodium is vital for maintaining body fluid homeostasis, which includes regulating the osmotic balance between the intracellular and extracellular environments[16,17]. Maintaining this balance is essential for proper cellular function and cell integrity[18]. Moreover, sodium, in conjunction with potassium, is essential for muscle contraction and relaxation, impacting both skeletal and cardiac muscles[19]. The healthy human tissue has an extracellular sodium concentration of ~140 mM and an intracellular sodium of ~10 mM[20,21], while they have an extracellular potassium concentration of 5 mM and an intracellular concentration of 140 mM[22] (**Figure 1.1**).

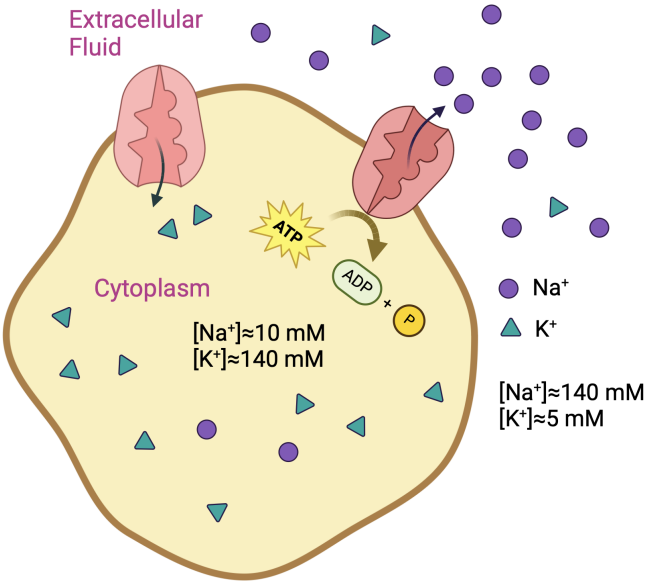

Figure 1.1: Intracellular and extracellular sodium and potassium distribution. This figure illustrates the differential distribution of sodium (Na^+) and potassium (K^+) ions across the cell membrane in healthy tissue. The extracellular fluid (ECF) is depicted with a significantly higher concentration of sodium ions, approximately 140 mM, compared to the intracellular fluid (cytoplasm), which contains around 10 mM of sodium[23]. Conversely, the intracellular fluid is rich in potassium ions, with a concentration of approximately 140 mM, while the extracellular fluid has about 5 mM of potassium ions[22]. The maintenance of these ion gradients is critical for various cellular functions and is primarily achieved through the activity of the sodium-potassium pump (illustrated in

pink). This pump actively transports sodium ions out of the cell and potassium ions into the cell, a process driven by the hydrolysis of adenosine triphosphate (ATP). During this ATP-dependent process, one ATP is consumed to move three sodium ions out of the cell and two potassium ions into the cell, resulting in the formation of adenosine diphosphate (ADP) and an inorganic phosphate (P). Image created with Biorender.com.

High dietary sodium intake has been shown to elevate blood pressure and negatively impact cardiovascular health, kidney function, and endothelial function[24]. Additionally, excessive salt intake is associated with increased inflammation in the body[25]. Given its multifaceted roles, the regulation of sodium levels is crucial for overall health and homeostasis, making it a key focus for understanding various health conditions.

Traditionally, the kidney was considered the primary organ responsible for sodium regulation[26]. However, emerging evidence has highlighted that skin serves not only as a protective barrier but also as an active participant in sodium homeostasis[27,28]. A study by Heer et al discovered that contrary to common belief, a high sodium diet increases plasma volume by shifting fluid from the interstitial space to the bloodstream without increasing total body water or body mass[29]. A study by Titze, including a 135-day terrestrial MIR simulator experiment (MIR stands for the Russian space station Mir, which was a modular space station that operated in low Earth orbit from 1986 to 2001), suggested that sodium can be stored in an osmotically inactive form, possibly in bone or connective tissue[30]. These findings challenge the conventional two-compartment model of sodium distribution, which states that total body water is partitioned between the intracellular component, comprising two-thirds, and the extracellular compartment, comprising one-third, with both compartments having similar osmolality[27]. Therefore, a

three-compartment model that incorporates the skin as a significant non-osmotic reservoir for sodium storage was proposed[31].

The skin might participate in the regulation of body sodium and water by buffering excessive dietary sodium[27]. Also, sodium gradients in the skin could create a hypertonic barrier that regulates fluid loss, similar to how countercurrent exchange systems work in the kidneys[28]. The skin's extracellular matrix is rich in GAGs, negatively charged molecules that 'bind' to positively charged sodium ions, creating a reservoir of osmotically inactive sodium[32]. This 'binding' mechanism allows the skin to store sodium without significantly affecting the osmotic balance[32], thereby acting as a buffer during dietary fluctuations. In the skin, macrophages can modulate the growth of lymph vessels through the release of vascular endothelial growth factor-C (VEGF-C)[33]. The growth of lymphatic vessels is believed to help the skin better transport and remove excess sodium from the tissue, which is considered the main process for removing excess sodium from the skin. In conditions of high sodium levels, extracellular sodium triggers the cyclooxygenase-2 (COX-2)/prostaglandin E2 (PGE2) pathway in dermal fibroblasts[34]. This activation leads to the production of GAGs, which enhances the skin's sodium storage capacity[35]. Additionally, increased sodium intake stimulates macrophages to express COX-2, further contributing to the regulation of sodium storage and release[36].

In addition to skin, the endothelial surface layer (ESL) is also likely involved in nonosmotic sodium storage. The ESL is a thin structure consisting of GAGs, proteoglycans and adsorbed plasma proteins, covering the inner surface of the endothelium[37] that lines the interior surface of blood vessels and lymphatic vessels. The

ESL can provide immediate intravascular sodium storage, unlike in the skin interstitium where sodium must be transported[27]. With a volume of approximately 1.5 liters in healthy individuals, the ESL can inactivate a significant amount of sodium immediately upon its entry to the circulation[38]. This three-compartment paradigm is illustrated in **Figure 1.2**.

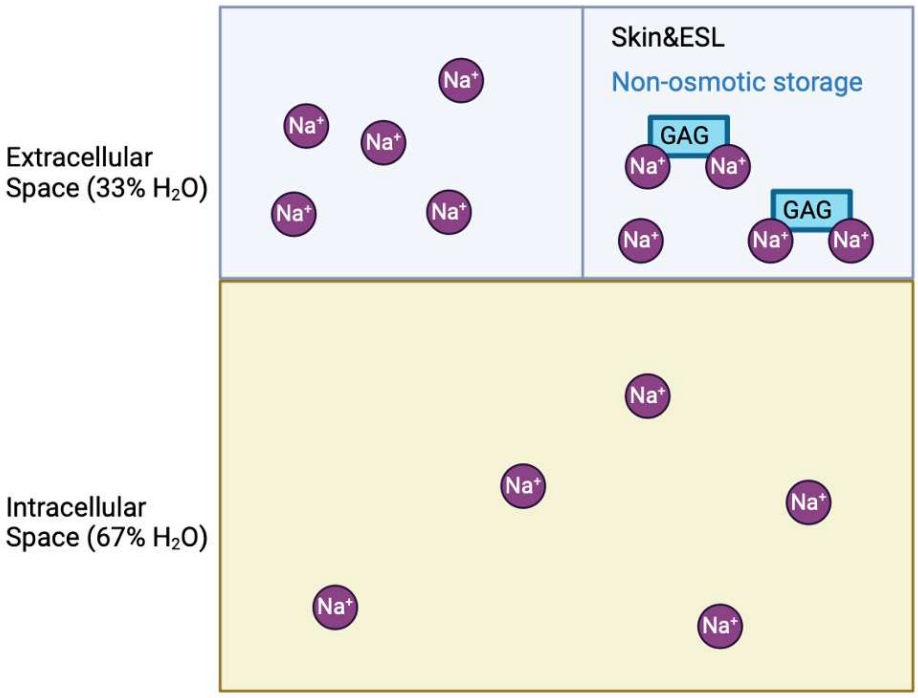

Figure 1.2: This paradigm challenges the traditional two-component theory that attributes sodium homeostasis primarily to kidney function. Traditionally, the kidney is viewed as the central organ responsible for maintaining sodium balance by excreting excess sodium. However, the three-compartment model offers a different perspective, suggesting that sodium is distributed across these spaces as follows: approximately 67% of sodium is located within the intracellular space, while 33% resides in the extracellular space. A key feature of this model is the concept of non-osmotic sodium storage, particularly in the skin and ESL. In this compartment, sodium ions can be stored by 'binding' to GAGs, as illustrated in the figure showing sodium ions 'binding' with GAGs within the skin and ESL. Image created with BioRender.com.

1.2.2 Skin Sodium Change in Pathological Conditions

Skin sodium levels have been found to change in various pathological conditions, indicating a potential link between sodium accumulation and disease progression[39]. Understanding these variations offers new insights into disease mechanisms and may lead to potential therapeutic approaches beyond traditional sodium intake management[40].

Previous sodium MRI studies have studied skin sodium levels in various pathological conditions. These conditions include dermatological conditions such as bacterial skin infection[41], lipedema[42–44] and psoriasis[45]; cardiovascular diseases such as hypertension[5,46,47] and acute heart failure[48]; type 2 diabetes mellitus (T2DM)[12,49,50]; autoimmune disease such as primary hyperaldosteronism (PHA)[8,51], cutaneous systemic sclerosis (SSc)[11], systemic lupus erythematosus (SLE)[52], primary adrenal insufficiency (PAI)[53] and multiple sclerosis[54]; kidney disease such as chronic kidney disease[9,55,56] and acute kidney injury[57]. Multiple studies also investigated skin sodium levels for patients undergoing dialysis[58–61] (**Table 1.1**). **Figure 1.3** presents sodium MRI images of a 24-year old normotensive man and an 85-year-old hypertensive man. The images are adapted from a 2013 study by Kopp[5], which focused on TSC and hypertension. This study was among the first to apply ^{23}Na MRI to calf skin, and its sodium MRI protocol has been widely accepted to investigate skin TSC and disease associations[5,8,9,11,12,41,46–50,52,54,57–59].

Table 1.1: Sodium MRI studies in skin in vivo which focused on skin sodium content and disease associations (grouped by various disorders).

Study	***Condition***	***Subjects***	***^{23}Na MRI Protocol***	***Main findings***
Jantsch 2015[41]	Bacterial skin infection	Bacterial skin infection patients (n=6).	Volume coil 3T 2D GRE sequence TA=13.7 min, TE=2.07 ms, TR=100 ms, FA=90° Resolution=3×3×30 mm^3 ***(denoted as 'Kopp Protocol')***	Skin TSC in the infected limb vs. the contralateral uninfected part: 96% ↑
Crescenzi 2018[42]	Lipedema	Lipedema patients (n=10) and controls (n=11).	Volume coil 3T 3D GRE sequence TA=15 min, TE=0.99 ms, TR=130 ms, FA=90° Resolution=3×3×30 mm^3	Skin TSC in lipedema vs. controls: 25% ↑ Subcutaneous adipose TSC in lipedema vs. controls: 27% ↑
Crescenzi 2020[43]	Lipedema	Lipedema patients (n=15) and controls (n=14).	Volume coil 3T 3D GRE sequence TA=15 min, TE=0.99 ms, TR=130 ms, FA=90° Resolution=3×3×30 mm^3	Skin TSC in lipedema patients vs. controls: 13% ↑ Calf skin TSC was significantly correlated with pain and lipedema stage.
Donahue 2022[44]	Lipedema	Stage 1-2 lipedema and early stage lipedema patients (n=5).	Volume coil 3T 3D GRE sequence TA=15 min, TE=0.99 ms, TR=130 ms, FA=90° Resolution=3×3×30 mm^3	Skin TSC in lipedema patients vs. before physical therapy: 9% ↓
Maifeld 2022[45]	Psoriasis	Psoriasis patients (n=18), controls (n=12).	Volume coil 3T 3D GRE sequence TA=15 min, TE=0.99 ms, TR=130 ms, FA=90° Resolution=3×3×30 mm^3	Skin TSC in psoriasis patients with PASI greater than 5 vs. controls: 24% ↑

Kopp 2013[5]	Hypertension	Hypertensive patients (n=57), controls (n=56).	*Kopp Protocol*	Skin TSC in women with refractory hypertension vs. controls: 29% ↑
Ott 2018[46]	Hypertension	Treatment resistant hypertension patients (n=41).	*Kopp Protocol*	Renal denervation did not change skin sodium content in treatment-resistant hypertensive skin.
Alsouqi 2022[47]	Hypertension	Hypertensive patients (n=60).	*Kopp Protocol*	Dietary salt restriction or diuretic intervention did not reduce skin and muscle sodium content over an 8-week period in patients with hypertension.
Hammon 2015[48]	Acute heart failure	Acute heart failure patients (n=9), controls (n=9).	*Kopp Protocol*	Skin TSC in acute heart failure patients before furosemide treatment:vs. controls: 106% ↑ Skin TSC in acute heart failure patients after furosemide treatment vs. controls: 53% ↑
Friedrich 2022[58]	Cardiovascular disease (CVD) patients on hemodialysis (HD)	HD patients with CVD history (n=23), HD patients without CVD history (n=29).	*Kopp Protocol*	Skin TSC in HD patients with previous CVD events vs. HD patients without CVD: 39% ↑ Muscle TSC in HD patients with previous CVD events vs. HD patients without CVD: 15% ↑
Kopp 2018[12]	T2DM	Hemodialysis patients without diabetes (n=30), type 2 diabetes hemodialysis patients (n=10).	*Kopp Protocol*	Skin TSC in T2DM vs. controls: 27% ↑
Karg 2018[50]	T2DM	Patients with type 2 diabetes (n=59).	*Kopp Protocol*	Skin TSC in T2DM after 6 weeks of dapagliflozin treatment vs. baseline: 6% ↓
Kannenkeril 2019[49]	T2DM	Patients with type 2 diabetes mellitus (n=59) and patients with primary arterial hypertension (n=33).	*Kopp Protocol*	Skin TSC in T2DM vs. primary hypertension: 19% ↑ Muscle TSC in T2DM vs. primary hypertension: 26% ↑

Kopp 2012[8]	PHA	PHA patients (n=5), controls (n=18)	*Kopp Protocol*	Muscle TSC in PHA vs. controls: 29% ↑ Skin TSC in PHA vs. controls: ↑ (numerically higher, but not statistically significant)
Kopp 2017[11]	SSc	Patients with diffuse cutaneous SSc (n=12) and controls (n=21).	*Kopp Protocol*	Skin TSC in fibrotic skin of SSc vs. healthy controls: 27% ↑ Skin TSC in fibrotic skin vs. non-fibrotic SSc skin: 36% ↑
Christa 2019[51]	PHA	PHA patients (n=6) and controls (n=8)	$^{1}H/^{23}Na$ Surface coil 3T 3D-GRE sequence TA=17 min, TE=2.01 ms, TR=100 ms, FA=90° Resolution=3.9×3.9×20 mm^3 for heart and muscle 1.3×11.8×30 mm^3 for skin	Skin TSC in PHA vs. controls: 39% ↑ Myocardium TSC in PHA vs. controls: 27% ↑ Calf muscle TSC in PHA vs. controls: 38% ↑
Carranza -leon 2020[52]	SLE	SLE patients (n=23), controls (n=28)	*Kopp Protocol*	Muscle TSC in SLE vs. controls: 19% ↑ Skin TSC in SLE vs. controls: ↑ (numerically higher, but not statistically significant)
Huhn 2021[54]	Multiple sclerosis	Male patients with relapsing remitting multiple sclerosis(RRMS) (n=29) and healthy controls (n=29).	*Kopp Protocol*	Skin TSC in male with RRMS vs. controls: 13%↑
Chifu 2022[53]	PAI	Longitudinal study: newly diagnosed PAI patients (n=8) and controls (n=8); Cross-sectional study: chronic PAI patients (n=22) and controls (n=22).	$^{1}H/^{23}Na$ Surface coil 3T 3D-GRE sequence TA=17 min, TE=2.01 ms, TR=100 ms, FA=90° Resolution 3.9×3.9×20 mm^3 for muscle 1.3×11.8×30mm^3 for skin	Skin TSC in first diagnosed PAI vs. controls before treatment: 25% ↓ Skin TSC in first diagnosed PAI vs. controls after treatment: similar levels

Dahlman 2015[59]	HD	Hemodialysis patients (n=24) and age-matched healthy controls (n=27).	*Kopp Protocol*	Skin TSC in end-stage renal disease vs. controls: 50%↑
Schneider 2017[9]	Chronic kidney disease(CKD)	Patients with mild to moderate CKD (n=99).	*Kopp Protocol*	Skin sodium is a strong independent predictor of left ventricular mass and is positively correlated with systolic blood pressure.
Hammon 2017[57]	Acute kidney injury (AKI)	AKI patients (n=7) and controls (n=14).	*Kopp Protocol*	Skin TSC in AKI before hemodialysis vs. control: 147%↑ Skin TSC in AKI after hemodialysis vs. control: 139%↑ Muscle TSC in AKI before hemodialysis vs. control: 97%↑ Muscle TSC in AKI after hemodialysis vs. control: 91%↑
Qirjazi 2021[55]	CKD	CKD patients (n=12), HD patients (n=13), and peritoneal dialysis (PD) patients (n=10), controls (n=20).	Volume coil 3T (Sequence not specified) TA=30 min, TE=1.2 ms, TR=100 ms, FA=90° Resolution=3×3×30 mm^3	Skin TSC in patients on HD vs. controls: 72%↑ Skin TSC in patients on PD vs. controls: 87%↑
Sahinoz 2021[60]	PD and maintenance hemodialysis (MHD)	MHD (n=33), PD (n=10), controls (n=119)	Volume coil 3T 2D GRE sequence TA=16 min, TE=0.99 ms, TR=130 ms, FA=90° Resolution=3×3×30 mm	Skin TSC in MHD vs. controls: +29% Skin TSC in PD vs. controls: +64%
Salerno 2022[61]	Dialysis	HD patients (n=52)	Volume coil 3T Density adapted 2D projection reconstruction, TA=30 min, TE=1.2 ms, TR=100 ms, FA=90° Resolution=3×3×30 mm^3	Higher skin sodium was associated with all-cause mortality and composite events.

Salerno 2023[56]	Pediatric CKD	Healthy pediatric participants (n=17), pediatric participants with CKD (n=19), and healthy adults (n=19).	Volume coil 3T Density adapted 2D projection reconstruction TA=30 min, TE=1.2 ms, TR=100 ms, FA=90° Resolution=3×3×30 mm^3	No significant skin sodium differences were found between healthy prediatric participants and CKD patients.

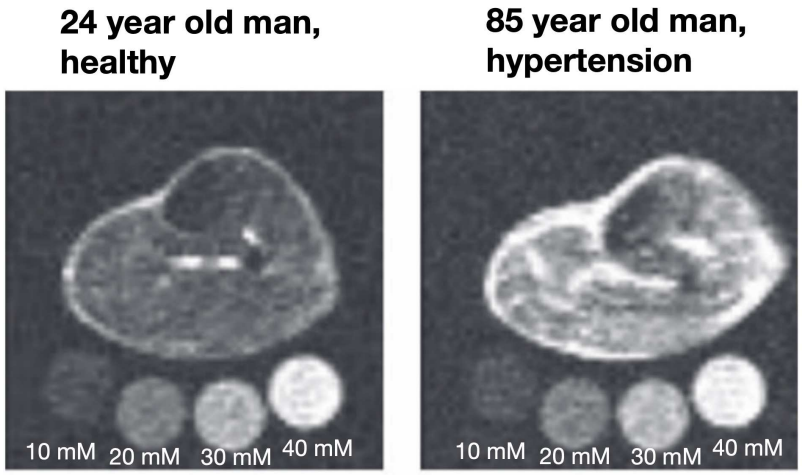

Figure 1.3: Comparison of sodium MRI scans of the calf muscle between a healthy 24-year-old man and an 85-year-old man with hypertension using the *Kopp protocol*. The images demonstrate visibly higher skin sodium concentration for the 85-year-old hypertensive man, with reference phantoms of 10 mM, 20 mM, 30 mM, and 40 mM sodium displayed below each scan for calibration. Figure adapted from *Kopp Hypertension 2013*[5].

Changes in skin sodium concentration in these pathologies could be due to various reasons. In atopic dermatitis, sodium levels are notably higher in affected skin areas compared to unaffected ones[62]. This elevation in sodium is linked to the development of the disease, particularly through mechanisms involving T-helper 2 (TH2) cells[62]. Similarly, in psoriasis, a chronic inflammatory dermatological disease, T-helper 17

(TH17) cells produce the cytokine IL-17, which is crucial for the disease's progression, and elevated skin sodium levels can exacerbate the inflammatory responses in psoriasis[45].

For patients with lipedema, the accumulation of lipid, sodium, and water results from impaired lymphatic vessel function, as a healthy lymphatic system is crucial for maintaining sodium balance within the skin[42–44].

Sodium storage in the skin could influence the renin-angiotensin-aldosterone system (RAAS), which regulates blood pressure and fluid balance and thus causes hypertension[63,64]. Reducing sodium intake can alter circulating microRNA expressions, which are associated with lower blood pressure and improved arterial compliance, which suggests a direct link between dietary sodium and cardiovascular health[65].

In PHA, excess aldosterone leads to increased sodium retention in the skin[51]. In SSc, fibroblasts release an increased amount of GAGs which lead to deposition of sodium[11]. Furthermore, a study on dialysis patients has demonstrated that sodium levels in human tissues can vary due to differences in glycosaminoglycan content[66]. This variation is linked to the differing expression levels of the enzyme XYLT-1 among individuals, which influences the amount of glycosaminoglycan present and thus influences sodium storage[66].

1.2.3 Skin Sodium Level in Healthy Controls

In addition to pathological conditions, skin sodium levels vary among healthy individuals. Investigating skin TSC levels in healthy controls is essential for establishing baseline data and providing a reference point for understanding sodium dysregulation.

Various studies have reported skin TSC measured by MRI protocols using volume coils and large voxels at 3×3×30 mm^3. A study from 2012 by Kopp et al[8] was among the first to investigate sodium MRI in human calf skin using a 2D gradient echo sequence, measuring skin TSC of approximately 18 mM in healthy females and 24 mM in healthy males[8]. Subsequent studies using similar methodologies (2D GRE, TE=2 ms, spatial resolution=3×3×30 mm^3) reported average calf skin sodium content varying between about 14 mM to 24 mM in healthy controls[5,11,48,52,57,60]. It is worth noting that most existing skin sodium MRI studies, including this one, focus on calf skin rather than other body parts due to several factors. Firstly, patient comfort is enhanced, and less movement artifact is likely when the subject is lying supine. Additionally, many studies have standardized the measurement of skin sodium in the calf, facilitating better comparison and reproducibility of results across different studies and populations.

Some research employed 3D GRE with a shorter TE (0.99 ms) than 2D GRE to measure skin sodium content in healthy individuals. For instance, Crescenzi et al. (2018) measured an average of 12 mM in healthy controls[42], while Crescenzi et al. (2020) reported 14 mM in the calf and 12 mM in the forearm[43].

Skin TSC quantification could benefit from utilizing a surface coil due to its high efficiency in areas close to the coil. A study by Linz utilized a 2D GRE sequence with

TE=2 ms and a 70 mm×64 mm surface coil, with a spatial resolution of 0.9×0.9×30 mm^3, measuring average skin TSC at approximately 53 mM in adult males[7] at 7T. However, these MRI-derived values are still generally lower than those measured by atomic absorption spectroscopy. For example, the study by Kopp et al. from 2012 used this technique to find skin sodium levels of 77 mmol/kg wet weight[8], roughly equivalent to 85 mM in calf skin in healthy controls (for a skin density of 1.1 kg/L[67]). Another study by Maifeld et al., which focused on psoriasis, measured skin sodium content in both healthy individuals and psoriasis patients using atomic absorption spectroscopy and found an average of 60 mM in healthy controls[45]. A comprehensive list of studies which quantified skin TSC using different MRI methods are shown in **Table 1.2**. As shown in the table, many studies using volume coil and GRE methods at 3T have measured average skin TSC in their respective cohorts at 12-21 mM, only one study using surface coil and a higher field strength at 7T[7] measured substantially higher average skin TSC of ~53 mM.

Studies have shown that skin sodium contents tend to be higher in men compared to women[5,8] and in older individuals compared to younger ones[5–7,59]. Studies that found a significant increase in skin TSC with aging or between males and females are denoted in **Table 1.3**. The age-related increase in skin sodium TSC may be linked to the progressive rise in blood pressure that accompanies the aging process[68].

The variability in skin sodium TSC among the healthy population may be influenced by differences in skin thickness between males and females, as well as changes in skin thickness with age. Studies have found that men typically have thicker skin than women[69–72] and that skin becomes thinner with age[72–74]. Average skin thickness of calf in healthy adults has been reported to range from 1.1 mm to 1.5 mm[72,75,76].

However, most existing sodium MRI protocols use large voxels (3×3×30 mm^3) relative to the actual skin thickness, leading to significant partial volume effects with adjacent air and adipose tissue, which has a 27% lower TSC than skin[42]. As a result, the age-related changes in TSC could be biased by variations in skin thickness. A study by Linz which used smaller voxels (0.9×0.9×30 mm^3) and surface coil imaging found a 24% increase in TSC with aging (25-53 years old)[7], while a study that used the 'Kopp' protocol with larger voxels (3×3×30 mm^3) reported a 53% increase in TSC over the same age range[5]. This finding suggests that using smaller voxels may result in more accurate (and potentially smaller) measurements of age- or sex-related increases in skin TSC.

Table 1.2: Skin sodium MRI studies which quantified absolute TSC values in healthy subjects (ordered by year of study).

Study	***Number of Controls***	***Imaging Part***	***^{23}Na MRI Protocol***	***Average skin TSC in controls***
Kopp 2012[8]	30	Calf	*Kopp Protocol*	21 mM
Kopp 2013[5]	56	Calf	*Kopp Protocol*	20 mM
Linz 2014[7]	17	Calf	Surface Coil 7T 2D-GRE sequence TA=10 min TE=2.3 ms TR=135 ms, FA=90° Resolution=0.9×0.9×30 mm^3	53 mM
Dahlman 2015[59]	27	Calf	*Kopp Protocol*	20 mM
Hammon 2015[48]	9	Calf	*Kopp Protocol*	21 mM
Kopp 2017[11]	21	Calf	*Kopp Protocol*	21 mM

Deger 2017[77]	8	Calf	Volume coil 3T 3D GRE sequence TA=15 min, TE=0.99 ms, TR=130 ms, FA=90° Resolution=3×3×30 mm^3	18 mM
Hammon 2017[57]	14	Calf	*Kopp Protocol*	18 mM
Crescenzi 2018[42]	11	Calf	Volume coil 3T 3D GRE sequence TA=15 min, TE=0.99 ms, TR=130 ms, FA=90° Resolution=3×3×30 mm^3	12 mM
Dyke 2018[6]	30	Calf	Volume coil 3T GRE sequence TA=15 min, TE=1.91 ms, TR=100 ms, FA=90° Resolution=3×3×30 mm^3	15 mM
Crescenzi 2020[43]	14	Calf and forearm	Volume coil 3T 3D GRE sequence TA=15 min, TE=0.99 ms, TR=130 ms, FA=90° Resolution=3×3×30 mm^3	Calf: 14 mM Forearm: 12 mM
Carranza-leon 2020[52]	28	Calf	*Kopp Protocol*	16 mM
Qirjazi 2020[55]	10	Calf	Volume coil 3T (Sequence not specified) TA=30 min, TE=1.2 ms, TR=100 ms, FA=90° Resolution=3×3×30 mm^3	19 mM
Sahinoz 2021[60]	119	Calf	Volume coil 3T 2D GRE sequence TA=16 min, TE=0.99 ms, TR=130 ms, FA=90° Resolution=3×3×30 mm	14 mM

Salerno 2023[56]	17	Calf	Volume coil 3T Density adapted 2D projection reconstruction TA=30 min, TE=1.2 ms, TR=100 ms, FA=90° Resolution=3×3×30 mm^3	14 mM

Table 1.3: Skin sodium MRI studies showing changes in TSC with demographic factors (sex or age) in healthy controls. Only healthy control subjects information are listed here in this table.

Study	***Subjects***	***^{23}Na MRI Protocol***	***Main findings***
Kopp 2012[8]	n=30, 17 males, age 62±7 years, 13 females, age 60±7 years	*Kopp Protocol*	Males have higher skin TSC than females (24 mM vs. 18 mM).
Kopp 2013[5]	n=56, males and females, age 22-90 years	*Kopp Protocol*	Males have higher skin TSC than females(24 mM vs. 18 mM). ↑skin TSC as age(youngest: 11 mM; oldest: 35 mM).
Linz 2014[7]	n=17, males only, age=46±18 (range: 20-80) years	Surface Coil 7T 2D-GRE sequence TA=10 min TE=2.3 ms TR=135 ms, FA=90° Resolution=0.9×0.9×30 mm^3	↑skin TSC as age(youngest: 45 mM; oldest: 56 mM).
Dahlman 2015[59]	n=27, 18 males and 9 females, age (<60 years): 44±10, age (>60 years): 69±7	*Kopp Protocol*	↑skin TSC as age (<60 years: 15 mM; >60 years20 mM).
Dyke 2018[6]	n=30, 15 males and 15 females, age 46±15 (range: 24-76) years	Volume coil 3T GRE sequence TA=15 min, TE=1.91 ms, TR=100 ms, FA=90° Resolution=3×3×30 mm^3	↑skin TSC as age (TSC vs. age not provided).

1.3 Introduction to Sodium MRI

1.3.1 Sodium Spin and Magnetization

MRI relies on the interaction of nuclear spins with externally applied magnetic fields. The source of MRI signals is rooted in certain nuclei having a net magnetic moment, which aligns with or against an applied static magnetic field B_0. In the presence of B_0, these nuclear spins can exist in either a lower energy parallel state or a higher energy antiparallel state relative to the field. The slight excess of spins in the lower energy state results in a net magnetization (M_0) along the direction of B_0. This net magnetization is the basis for generating MRI signals. This process allows the nuclei to behave in unison, making it possible to detect their reaction to a perturbation. For a nucleus to respond to this perturbation and to be viable to NMR, it must have a non-zero spin quantum number ($I \neq 0$).

The spin quantum number for a nucleus is determined by the number of protons and neutrons it contains. Nuclei with even numbers of both protons and neutrons exhibit a spin quantum number of $I = 0$ due to pairing effects (e.g., ^{12}C). Nuclei with odd numbers of both protons and neutrons possess spin quantum numbers that are positive integers (e.g., ^{2}H, ^{14}N). Most isotopes, however, have either even/odd numbers of protons and neutrons or odd/even numbers of protons and neutrons. These nuclei would have spin quantum numbers that are half-integer values (**Table 1.4**).

The spin state of each nucleus is intricately linked to its spin quantum number. For a nucleus with a spin I, the possible spin states range from -I to I in integer steps. For example, a nucleus with $I = \frac{1}{2}$ has two spin states: $\frac{1}{2}$ and $-\frac{1}{2}$. This is the case for ^{1}H,

which is prevalent in the human body. On the other hand, ^{23}Na, which has 11 protons and 12 neutrons, possesses a spin quantum number of $\frac{3}{2}$. Consequently, ^{23}Na has four spin states: $-\frac{3}{2}, -\frac{1}{2}, \frac{1}{2}, \frac{3}{2}$. Because sodium has these four energy levels, there would be more scenarios for energy transitions for sodium MRI than proton MRI.

A spin can shift between two neighboring energy levels, a process known as a single quantum transition. Additionally, transitions can occur between different states, involving double or triple quantum changes (**Figure 1.4**). In fluids that contain sodium, such as saline, only single quantum transitions are observed, resulting in a simple single-line spectrum as all single-quantum transitions have the same energy. However, in highly ordered environments such as gels (e.g. agar gel or gellan gel), or some biological tissues such as cartilage, the energy gaps between quantum states of ^{23}Na shift due to anisotropy. This variation occurs when Na^+ ions interact with ordered molecules. Consequently, the spectrum will exhibit a central peak and two satellite peaks, separated by the quadrupole frequency ω_Q.

In addition to spin angular momentum I, another critical parameter is the nuclear magnetic moment μ. The nucleus precesses around the B_0 field, with the direction and frequency of this precession determined by the alignment of μ with the external magnetic field. The gyromagnetic ratio γ of a nucleus is defined by the equation:

$$\gamma = \frac{2\pi\mu}{Ih} \tag{1.1}$$

where h is the Planck constant. The spin quantum numbers, proton/neutron counts, and gyromagnetic ratios of some common nuclei are detailed in **Table 1.4**.

When subjected to the B_0 field, nuclei precess at a specific frequency known as the Larmor frequency (ω_0), given by:

$$\omega_0 = \gamma B_0 \quad (1.2)$$

At B_0=3 T, the Larmor frequency of ^{23}Na would be 33.8 MHz, whereas at 4.7 T the Larmor frequency of ^{23}Na would be 52.9 MHz.

During an MRI acquisition, an additional oscillating magnetic field B_1, which is applied perpendicular to the B_0 field, is introduced. The B_1 field perturbs the nuclei, causing the net magnetization to flip away from the z axis and towards the x-y plane. This angular displacement of M_0 is defined as

$$\alpha = \gamma B_1 t_{rf} \quad (1.3)$$

where t_{rf} is the RF pulse duration.

Table 1.4: Spin number, number of protons and neutrons, and gyromagnetic ratios for some nuclei commonly found in biological tissues.

Nucleus	***Spin(I)***	***Number of protons/Number of neutrons***	***Gyromagnetic Ratio γ (MHz/T)***
^{1}H	1/2	1/0	42.58
^{13}C	1/2	6/7	10.71
^{14}N	1	7/7	3.08
^{23}Na	3/2	11/12	11.26
^{31}P	1/2	15/16	17.24
^{35}Cl	3/2	17/18	4.18
^{39}K	3/2	19/20	1.99

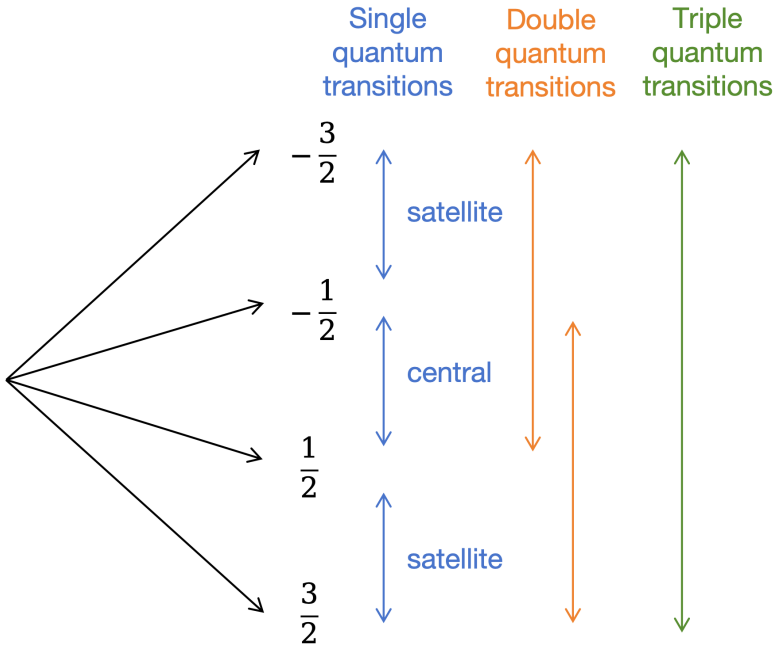

Figure 1.4: Energy state transitions of sodium nucleus spin. These transitions include single quantum transitions (blue arrows), double quantum transitions (orange arrows) and triple quantum transitions (green arrow).

1.3.2 Sodium Relaxation In Vivo

During MRI, M_0 is initially rotated away from the z-axis by the RF pulse. The component of M_0 projected onto the x-y plane, known as transverse magnetization (M_{xy}), forms the basis of the signal detected in NMR acquisition. After RF excitation, M_{xy} begins to decay, and simultaneously the longitudinal magnetization (M_z) starts to recover. The recovery of M_z is characterized by the longitudinal relaxation (spin-lattice relaxation) time constant T_1. Transverse relaxation, also known as spin-spin relaxation, results from the dephasing of the precessional phases of individual magnetic dipoles within the tissue. The

transverse relaxation time constant is T_2. The relaxation behavior of ^1H can be described in exponential decay equations:

$$M_z(t) = M_0(1 - e^{-\frac{t}{T_1}}) \quad (1.4)$$

$$M_{xy}(t) = M_0 e^{-\frac{t}{T_2}} \quad (1.5)$$

A non-uniform local magnetic field, however, can alter the local static field and cause T_2 relaxation to happen more rapidly. The apparent transverse relaxation time (T_2^*) accounts for the dephasing process and is related to T_2 by this equation:

$$\frac{1}{T_2^*} = \frac{1}{T_2} + \frac{1}{T_2'} \quad (1.6)$$

where T_2' is the relaxation time constant attributable to local magnetic field inhomogeneities.

In saline solutions, sodium relaxation is monoexponential because all possible single-quantum transitions in water have the same energy. However, in biological tissues, sodium relaxation is biexponential due to the presence of spin 3/2[78]. This leads to a biexponential decay for transverse magnetizations and also a biexponential recovery for longitudinal magnetizations in biological tissues[79].

For T_2 relaxation, a 60/40 ratio of fast (T_{2fast}) to slow (T_{2slow}) components is present when assuming a homogeneous environment. Although T_1 relaxation is theoretically biexponential as well[80], the fast component is usually negligible (~20%), so most sodium T_1 relaxation studies report using monoexponential models (**Figure 1.5**).

The transverse relaxation decay and longitudinal relaxation recovery for ^{23}Na in vivo, assuming a homogeneous environment, are given by:

$$M_z(t) = M_0(1 - e^{-\frac{t}{T_1}}) \quad (1.7)$$

$$M_{xy}(t) = M_0(0.6 * e^{-\frac{t}{T_{2fast}}} + 0.4 * e^{-\frac{t}{T_{2slow}}}) \quad (1.8)$$

A summary of sodium relaxometry measurements for various human tissues in vivo is presented in **Table 1.5**. T_1 values range from 20 ms in knee cartilage to 39 ms in brain[81,82]. T_{2fast} values span from as low as 0.17 ms in skin to 2.4 ms in brain[83,84], while T_{2slow} values span from as low as 7.6 ms in skin to 32 ms in brain[7,84]. Skin tends to exhibit shorter T_{2fast} values compared to more hydrated tissues such as brain and muscle (see **Table 1.5**), which further highlights the importance of using short TE sequences to minimize signal loss when imaging the skin.

Table 1.5: Summary of sodium relaxometry in vivo. This table provides a comparative summary of the relaxation times T_1, T_{2fast}, and T_{2slow} for various body tissues, as reported by different studies conducted at various magnetic field strengths.

Body Tissue	***Study/B_0 field***	***T_1***	***T_2***
Knee Cartilage	Madelin 2012/7T[81]	20 ms	T_{2fast}: 0.5 ms-1.4 ms T_{2slow}:11.4 ms-14.8 ms
Knee Cartilage	Feldman 2013/4.7T[85]	21 ms	T_{2fast}=0.8 ms T_{2slow}=19.7 ms
Muscle	Kordzadeh 2020/4.7T[86]	N/A	T_{2fast}=1.6 ms T_{2slow}=16.1 ms
Skin	Stobbe 2023/4.7T[83]	N/A	T_{2fast}=0.17 ms T_{2slow}=12.5 ms
Skin	Kordzadeh 2020/4.7T[86]	N/A	T_{2fast}=0.4 ms T_{2slow}=9.3 ms

Skin	Linz 2014 /7T[7]	27 ms	T_{2fast}=0.5 ms T_{2slow}=7.6 ms
Brain	Coste 2019/3T[82]	39 ms	N/A
Brain	Worthoff 2019/4T[84]	N/A	T_{2fast}=2.4 ms T_{2slow}=32 ms

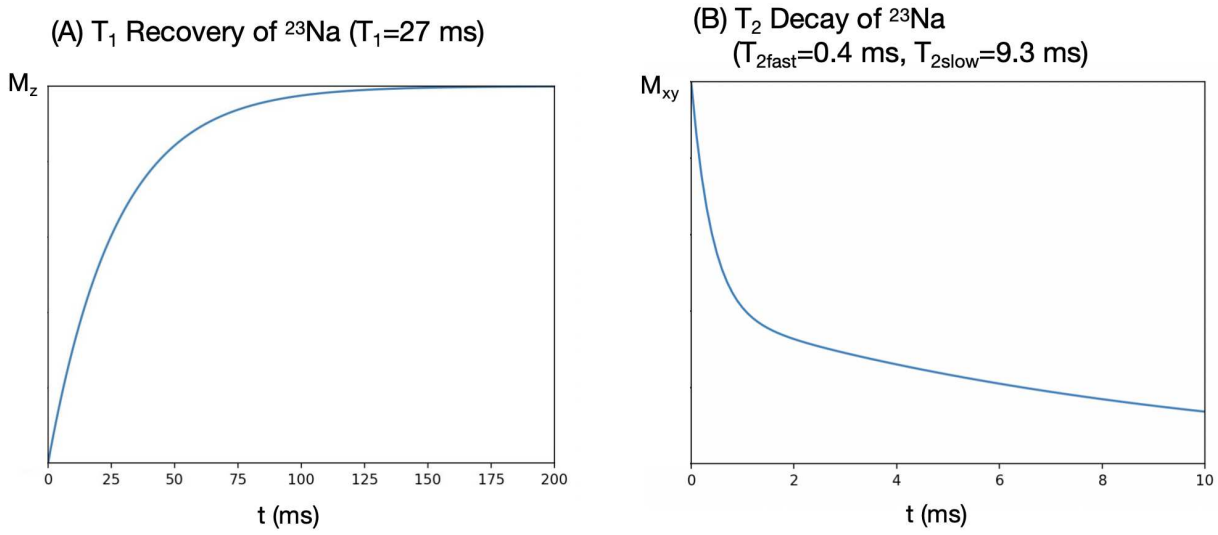

Figure 1.5: Illustration of ^{23}Na MRI relaxation decay plotted using measurements from previous studies by Linz (2014)[7]**(A)** and Kordzadeh (2020)[86]**(B)**. In this figure, t represents time after 90° RF pulse. **(A)**Monoexponential longitudinal relaxation decay (T_1=27 ms)[7], 95% of the signal is recovered at t=85 ms. **(B)** Biexponential transverse relaxation decay (T_{2fast}(60%)=0.4 ms, T_{2slow}(40%)=9.3 ms)[86]. The biexponential T_2 decay occurs much more rapidly than the T_2 decay of ^{1}H, with 59% of the signal dropped at t=1 ms, and 68% of the signal dropped at t=2 ms.

1.4 Skin Sodium MRI Applications

1.4.1 Sequences Used for Skin Sodium MRI

GRE is one of the most readily available and straightforward sequences for sodium MRI. It can be adapted from existing ^{1}H MRI sequences found on most platforms, which makes GRE a practical initial choice for sodium imaging[87].

However, the minimum TE allowed for GRE sequences is 1-2 ms, which makes it challenging to capture adequate signal due to the rapid bi-exponential decay of ^{23}Na (**Figure 1.5**). Ultrashort sequences could address this limitation. Short TE smaller than 1 ms can be obtained through non-cartesian trajectories such as radial or spiral k-space trajectories, which start data acquisition at the center of k space[20]. Examples of radial trajectories include 3D radial sequence[88] and density adapted radial sequence[89]. Spiral trajectories sample more of k-space with each projection, enhancing their sampling efficiency and consequently reducing scan time[90]. Examples of these spiral sequences include TPI[91] and 3D cones[92].

A notable study conducted in 2014, utilizing a 9.4 Tesla magnetic field strength, compared the performance of five different imaging sequences: TPI, 3D radial imaging, density adapted 3D radial imaging, 3D Cones, TPI, and GRE. Among these sequences, TPI demonstrated the superior capability for quantifying sodium content in the brain[93].

In this study, the TPI sequence was implemented. TPI is a rapid three-dimensional imaging technique characterized by a consistent sampling density. It is distinguished by

rapid and uniform sampling of a spherical volume in k-space, which can minimize noise transferred into the image domain[94].

The TPI trajectory begins radially at the center of k-space and extends along a cone angle θ, twisting along the surface of the cone to reach the maximum k-space value (K_{max})[94]. The illustration of k-space trajectory of TPI and TPI pulse sequence are demonstrated in **Figure 1.6** and **Figure 1.7**.

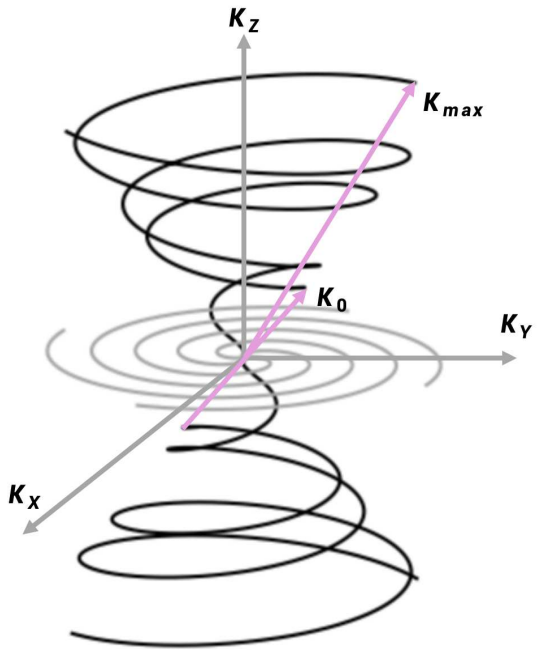

Figure 1.6: K-space trajectories of TPI sequence.

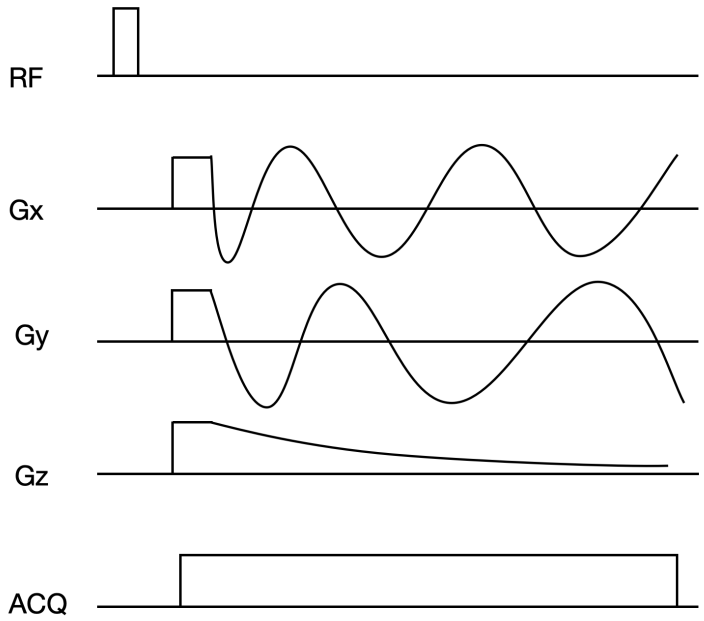

Figure 1.7: 3D-TPI pulse sequence. The initial 'flat' component of Gx, Gy and Gz compose the 'center-out' portion of each TPI k-space trajectory.

1.4.2 Hardware Used for Skin Sodium MRI

In MRI, RF coils are used to transmit RF energy and receive the MR signal[95]. Often, particularly in sodium MRI, the same RF coil functions as both the transmit (Tx) and the receive (Rx) coil. During transmission, the RF coil generates an electromagnetic field oscillating at ω_0. A volume RF coil is often used to produce a more uniform B1 field within the field-of-view (FOV). Other types of coils, such as surface coils, may produce a less uniform B_1 field, resulting in varying excitation profiles. When the spins in the sample are excited, they generate an oscillating magnetic field, which induces an electric current in the RF coil. This current is then detected by the RF coil during the reception phase to capture the MR signal. X-nuclei imaging typically requires the use of

custom-built RF coils because X-nuclei resonate at different frequencies than protons. Plus, X-nuclei are generally far less abundant than protons, which often requires careful consideration of the coil's geometry to maximize SNR in the tissue of interest.

RF coils can be seen as a simple RLC circuit, and the resonant frequency can be described as:

$$\omega = \frac{1}{\sqrt{LC}} \tag{1.9}$$

Where L is the inductance and C is the capacitance. For ^{23}Na MRI at 4.7T, the coil should be tuned to 52.9 MHz. And when the coil is tuned to Larmor frequency, f_0 can be determined as

$$f_0 = \frac{1}{2\pi\sqrt{LC}} \tag{1.10}$$

The quality factor (Q factor) is a parameter used to measure the coil's sensitivity and efficiency in detecting MR signal[96]. Q factor of a RLC circuit is defined as

$$Q = \frac{2\pi f_0 L}{R} = \frac{1}{R}\sqrt{\frac{L}{C}}_{95} \tag{1.11}$$

In practice, the Q factor is usually measured by the equation below, where B is the -3 dB coil bandwidth.

$$Q = \frac{f_0}{B} \tag{1.12}$$

High Q factors in RF coils are indicative of narrow bandwidth, which means the coil can operate efficiently at a specific frequency with minimal energy loss, essential for enhancing SNR and sensitivity in imaging.

When testing the coil, both loaded Q factor (Q_{loaded}) and unloaded factor Q ($Q_{unloaded}$) should be tested. The ratio of $Q_{unloaded}$ and Q_{loaded} is defined as:

$$r = \frac{Q_{unloaded}}{Q_{loaded}} \tag{1.13}$$

The r value can indicate coil sensitivity. $Q_{unloaded}$ is always bigger than Q_{loaded}, so r is always bigger than 1. A higher r value suggests that the coil maintains good performance even when loaded with a sample.

The most commonly used types of coils for skin ^{23}Na imaging are birdcage coils and surface coils. Birdcage coils are particularly widely used due to its homogeneous RF field in the volume of interest and larger volume coverage. Plus, birdcage coils are generally more readily available. In contrast, surface coils are generally preferred for their high SNR in regions close to the coil and their ability to be tailored to specific anatomical regions. Surface coils are often used in applications requiring high-resolution imaging of superficial structures. However, the two dimensional design of surface coils leads to a non-uniform, transmit and receive profile. Images acquired with surface coils can exhibit high SNR near the coil but have a rapid signal drop-off with increased distance. Surface coil arrays can extend the effective imaging volume, allowing for high sensitivity coverage over a larger area[97]. Most existing studies have used volume coils for skin sodium imaging, however, some more recent research has been utilizing surface coils.

Giovannetti (2014)[98] used spectroscopy to propose the design of a circular transmit-receive single loop surface coil (diameter=25 cm) and demonstrated its feasibility across various tissues, including the calf, brain, kidney, and heart, although

specific tissue sodium concentration (TSC) numbers were not provided. Linz (2014)[7] measured the mean skin TSC in adult males at ~53 mM at 7T with a two-loop surface coil (each outer loop size is 7 cm×6 cm), which is more than twice as high as values obtained from low-resolution volume coil studies. Christa (2019)[51] used a receive coil of 17 cm×14 cm, and employed flat voxels with small dimensions across the skin and detected a 39% increase in skin TSC in PHA patients compared with controls, a result not observed with the Kopp method (Kopp, 2012)[8], potentially due to reduced partial volume effects. Milani (2019)[99] used a single loop surface coil with the diameter of 14 cm, compared 2D GRE and UTE protocols for imaging upper leg muscle and skin, concluding that the GRE protocol yielded higher SNR, while UTE was necessary for T_{2fast} and T_{2slow} quantification and for detecting small sodium amounts. Chifu (2022)[53] used the same protocol as Christa (2019) and found that, in newly diagnosed patients, tissue sodium was initially reduced but significantly increased after treatment in muscle and skin, although no TSC numbers were provided. Although the application of surface coils to measure skin TSC is promising, there are currently limited studies in this area, with the study by Linz (2014) being the only one to provide absolute TSC numbers. **Table 1.4** lists past studies that have applied surface coil on sodium imaging of the skin.

Table 1.6: Studies that applied surface coil in sodium MRI on skin.

Study/Surface coil used in the study	***Subjects***	***Body Part***	***^{23}Na MRI Protocol***	***Main Findings***
Giovannetti 2014[98] Transmit-receive ^{23}Na single loop surface coil, 25 cm diameter	Healthy volunteer(not specified)	Calf, brain, kidney, and heart	3T FID-CSI(Free induction decay chemical shift imaging) TR=480 ms TA=5 min 7 s Resolution=1.6×1.6×20 mm^3 (Calf) Resolution=2.4×2.4×40 mm^3 (Brain) Resolution=2.5×2.5×40 mm^3 (Kidney) Resolution=2.7×2.7×25 mm^3 (Heart)	Proposed the design of a circular transmit-receive surface coil.
Linz 2014[7] Transmit-receive ^{23}Na two loop surface coil, each with an outer loop size of 70 mm×64 mm and a conductor width of 12 mm.	Healthy male adult volunteers (n = 17)	Calf	7T 2D-GRE sequence TA=10 min TE=2.3 ms TR=135 ms, FA=90° Resolution=0.9×0.9×30 mm^3	Feasibility study of applying surface coil to measure skin TSC. Skin sodium concentration correlates with age.
Christa 2019[51] Dual tuned ^{1}H/^{23}Na surface coil: ^{23}Na transmit coil (single loop 280×175 mm), and a combination of a loop (170×135 mm) and an 8-shaped coil for reception	8 PHA patients and 12 normotensive healthy controls	Heart, calf muscle and skin	3T 3D-GRE sequence TA=17 min, TE=2.01 ms, TR=100 ms, FA=90° Resolution=3.9×3.9×20 mm^3 for heart and muscle 1.3×11.8×30mm^3 for skin	Compared to healthy control, PHA patients had higher sodium content in their myocardium, calf muscle and skin.
Milani 2019[99] A transmit-receive sodium surface coil, single loop, diameter=14 cm	Healthy controls (n=11)	Upper leg	3T GRE sequence: TR=100 ms TE=1.73 ms TA=13.25 min	GRE protocol yielded higher SNR than UTE protocol, however,

			Resolution=4.7×4.7×33 mm^3 UTE sequence: TE=0.2 ms TR=100 ms TA=13.20 min Resolution=4.7×4.7×4.7 mm^3	for T_{2fast} and T_{2slow} quantification and quantifying small amounts of sodium, UTE is needed.
Chifu 2022[53] Dual tuned $^{1}H/^{23}Na$ surface coil: ^{23}Na transmit coil (single loop 280×175 mm), and a combination of a loop (170×135 mm) and an 8-shaped coil for reception	A longitudinal study on 8 patients newly diagnosed with PAI, and 8 matched healthy controls. A cross-sectional study with 22 patients with chronic PAI and 22 matched healthy controls.	Calf	3T 3D-GRE sequence TA=17 min, TE=2.01 ms, TR=100 ms, FA=90° Resolution $3.9×3.9×20\ mm^3$ for muscle $1.3×11.8×30mm^3$ for skin	In newly diagnosed patients, tissue sodium was reduced and significantly increased after treatment in muscle and skin.

1.4.3 B_1 Correction

B_1 correction in sodium MRI is essential for improving the accuracy of sodium concentration maps by mitigating the effects of B_1 inhomogeneity. The B_1 field consists of two components: B_1^+ and B_1^-. The B_1^+ field refers to the transmit RF field, while the $B1^-$ component refers to the reception RF field, which detects the resulting MR signal. B_1^+ determines flip angle α_{actual} and B_1^- affects the sensitivity of the coil in detecting MR signal. Variations in B_1^+ field can lead to non-uniform actual flip angles across the imaging volume. This non-uniformity results in inaccurate signal intensities, thereby compromising the reliability of the obtained images. B_1 correction is essential to achieve accurate and quantitative sodium MRI data.

Typically, B_1 mapping falls into two categories, which is signal magnitude-based or signal phase-based, while most methods are based on the alteration of signal

magnitude[100]. The conventional approach for B_1^+ mapping is to use a double-angle method (DAM). This method involved acquiring two images with flip angles of α and 2α. Actual flip angle α_{actual} can be calculated with the signal intensities acquired from these two images. The signal intensities in the two images can be described as:

$$\frac{S_{2\alpha}}{S_{\alpha}} = \frac{sin(2\alpha_{actual})}{sin(\alpha_{actual})} \tag{1.14}$$

And given the trigonometric identity $sin(2\alpha) = 2sin(\alpha)cos(\alpha)$, one can get:

$$\frac{S_{2\alpha}}{S_{\alpha}} = 2cos(\alpha_{actual}) \tag{1.15}$$

And then the α_{actual} can be solved from the equation above. The relative B_1^+ (rB_1^+) for a point of tissue would be $\frac{\alpha_{actual}}{\alpha_{nominal}}$. With α_{actual} being the actual flip angle and $\alpha_{nominal}$ being the prescribed flip angle. This DAM B_1 mapping method is relatively simple and is broadly available[101].

One commonly-used phase-based B_1^+ mapping method is the Bloch-Siegert off-resonance (BLOSI) method[100]. This method was reported to be faster and independent of T_1 effects and yields higher SNR than the double-angle approach. BLOSI has been reported to offer several advantages over the double angle method. Following the RF excitation pulse, the Bloch–Siegert pulse induces a B_1^+ dependent phase shift. Notably, BLOSI is faster, as it does not depend on T_1 relaxation effects[102]. Additionally, this method provides a higher SNR compared to the double angle approach[103]. A study by Vaeggemose et al demonstrated that the BLOSI B_1 field correction method is clinically feasible and

time-efficient for sodium imaging on multiple tissues including the brain, heart, kidney, and thigh muscle[104].

The phase shift caused by the Bloch-Siegert effect can be described as:

$$\varphi_{BS} = B_{1,peak}^{2} \int_{0}^{T} \frac{(\gamma B_{1,normalized}(t))^{2}}{2\omega_{RF}(t)} dt = B_{1,peak}^{2} \cdot K_{BS}^{104} \quad (1.16)$$

$$B_1(t) = B_{1,peak} \cdot B_{1,normalized}(t)^{104} \quad (1.17)$$

K_{BS} is a constant that characterizes the phase shift induced by a specific RF pulse, $B_{1,peak}$ and represents the magnitude of the maximum point in the RF waveform[100].

By performing at least two acquisitions with the Bloch–Siegert off-resonance frequency applied in both positive and negative directions, it is possible to eliminate undesired phase effects originating from other sources. This process allows for the accurate measurement of the B_1^+ field[100].

1.5 Project Aims and Hypothesis

This study aims to enhance the accuracy of skin sodium quantification through the application of novel sodium MRI techniques. The primary objective is to reduce signal measurement error by employing an SNR-efficient surface coil, reshaping voxels to match the unique anatomy of the skin, and utilizing a TPI sequence with a short TE. Furthermore, skin thickness measurements will be conducted using ^{1}H anatomical images to investigate potential correlations between skin thickness and TSC. In addition, the

study will examine possible correlations between age, sex, and skin TSC to understand demographic influences on sodium accumulation. The central hypothesis is that these methodological advancements will result in a more accurate estimation of skin TSC. Moreover, this thesis proposes a robust and efficient methodology for quantifying skin TSC for future research.

2. Methodology

This chapter elaborates on the preliminary experiments and experimental procedures, offering more detail than the main results discussed in Chapter 3.

2.1 Participants

A total number of 14 healthy adults (aged 21 – 61 years, 8 male, 6 female) were recruited, and informed written consent was received for each participant. Demographic information such as age, height, and weight was recorded at the time of MRI.

Inclusion criteria mandated that participants be free from any preexisting chronic conditions known to potentially influence or alter skin tissue sodium concentration measurements.

2.2 Experiment Setup

All sodium images were acquired on a Varian Inova (Palo Alto, CA, USA) 4.7 T scanner, using VnmrJ 1.1 D. The gradient amplifier has maximum gradient capabilities of 60 mT/m.

2.2.1 Volume Coil Setup

For volume coil imaging, the left leg of each participant was positioned within a single-tuned 12 rung birdcage transmit-receive knee volume coil (diameter = 17.8 cm, length = 10 cm). This coil was selected in order to mimic the commonly used volume coil protocol for existing skin sodium MRI studies.

To position the participant's leg, the volume coil was set up in a manner that allowed the calf to rest comfortably and securely within the coil. The participant lay supine on the scanner table, and the leg was gently inserted into the coil, ensuring that the knee was centrally aligned. Proper alignment was verified to maintain consistent field distribution and image quality across all participants.

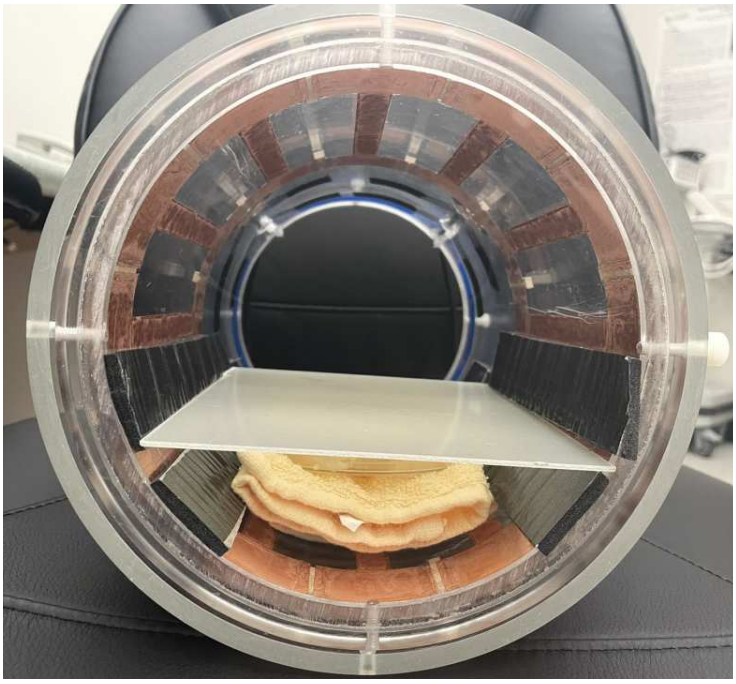

Figure 2.1: Experiment setup for volume coil imaging. The space inside the volume coil allows for the calf to rest on a platform and an agar phantom was placed on the bottom of the platform.

2.2.2 Surface Coil Setup

A transmit-receive surface coil with a diameter of 5 cm was employed in this study. The size of the coil was selected because it ensured that the calf section being imaged fully covers the coil. The surface coil was placed in a custom-cut foam piece to elevate the coil

to the same height as the iso-center, and pieces of custom-cut fiberglass were used to separate the surface coil, skin and agar calibration phantom to ensure symmetric B_1 on both sides (**Figure 2.2**). A reference line was drawn from left to right along the thickest part of the calf, serving as a consistent marker for the imaging location throughout the experiment. This reference line was maintained for all sodium MRI and proton MRI acquisitions. During the sodium MRI sessions, the reference line was carefully aligned with the center of the surface coil, guaranteeing that the region of interest was optimally positioned within the coil's sensitive area. The surface coil setup is illustrated in **Figure 2.3**.

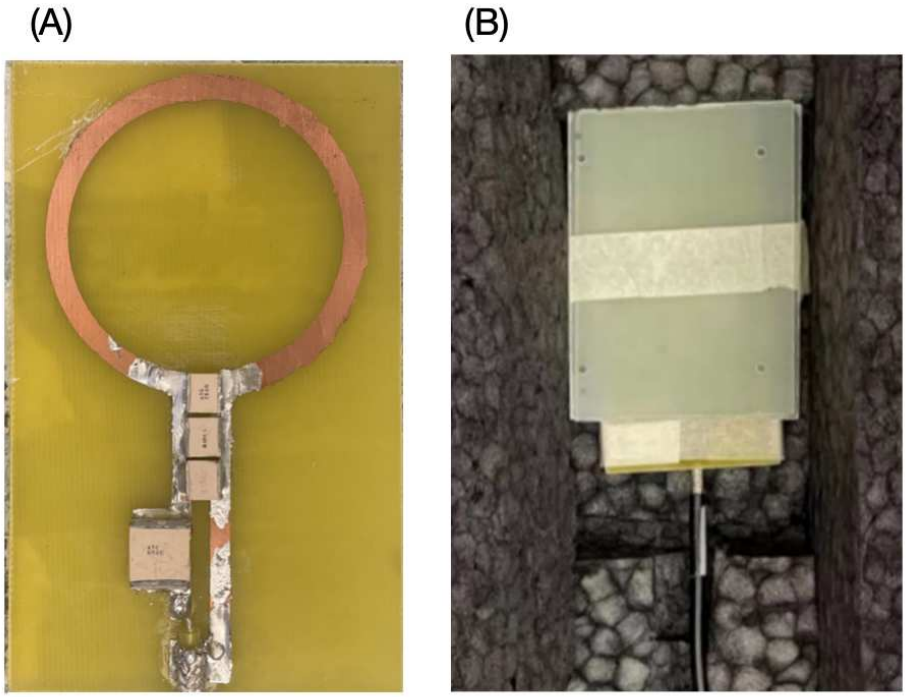

Figure 2.2: (A) The single-loop surface coil (diameter=5 cm) used in this thesis. **(B)**The surface coil (with fiberglass spacers to separate the coil from calf skin/agar) setup. The numbers of fiberglass pieces on each side of the coil were chosen to ensure B_1 equivalent surface on each side.

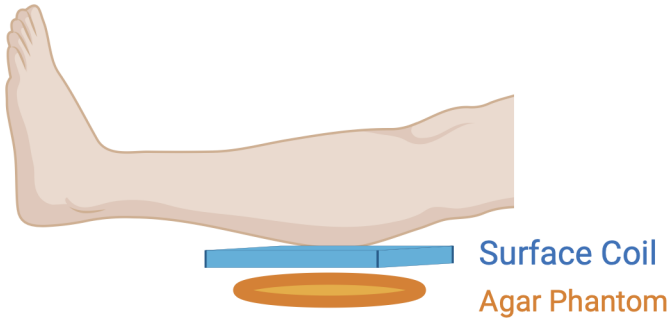

Figure 2.3: An illustration of the surface coil setup for calf skin imaging in this thesis.

2.2.3 Phantom Construction and Calibration

In this study, phantoms were constructed to facilitate the quantification of skin sodium content. Phantoms used for this study were made using a mixture of agar powder, a gelatinous substance that can be easily molded, and has electrical properties similar to human skin (SELECT Agar by Invitrogen), water, and sodium chloride (sodium chloride crystalline powder PDV, 99+% by Thermo Scientific).

Specifically, 12.5 g of agar powder was added to 250 ml of H_2O to create a 5% agar mixture. To this mixture, 0.35 g (6 mmol, which equals 24 mM in a 250 ml solution) of NaCl was added. The mixture was heated in a microwave at low power to minimize air content and water evaporation, with small amounts of water added to compensate for any water loss. It is important to note that the sodium concentration in the agar powder is unknown. This agar phantom was constructed to achieve a target sodium concentration of

60 mM, and the exact sodium concentration was measured during phantom calibration. The mixture was then poured into a petri dish (10 mm in height, 92 mm in diameter) and sealed with plastic bonder. A saline solution of 50 mM NaCl was prepared and poured into a petri dish of the same size.

The phantom was calibrated using both the *VolPencil* protocol and *SurfPancake* protocol (details described in Chapter 2.4), both with flip angle of 90° and TR=200 ms. For volume coil imaging, the agar phantom and the B_1 equivalency in agar and saline for surface coil imaging were tested prior to calibration. A longer repetition time (TR) of 200 ms was selected because T_1 in 5% agar gel is 36 ms and T1 in saline is at 55 ms[105]. The signal intensities of the agar phantom and saline were compared to determine the sodium concentration in the agar phantom, which was constructed to have a sodium concentration of 60 mM. A representative agar phantom calibration image is shown in **Figure 2.4**.

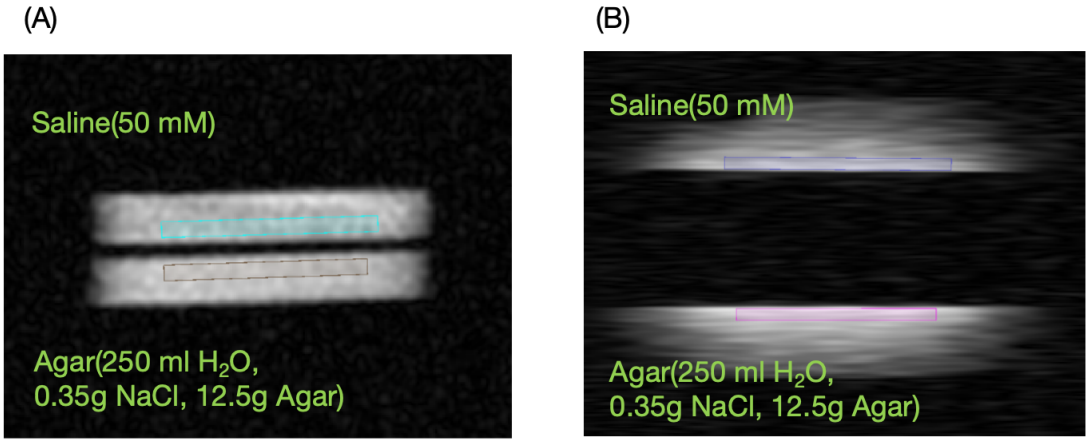

Figure 2.4: Calibration of sodium MRI phantoms using different imaging coils. (A) shows the results from a volume coil and (B) from a surface coil. Both utilize a 50 mM saline solution as the reference at the top and feature an agar phantom at the bottom (comprising 250 mL H_2O, 0.35g NaCl, 12.5g Agar). Each imaging technique demonstrates consistent sodium detection of 60 mM Na^+ in the agar gel.

2.3 Preliminary Experiments

2.3.1 Surface Coil Symmetric B_1 Experiments

To determine the B_1 equivalent surfaces, symmetric B_1 was verified using two agar phantoms with the same size and sodium concentration. To verify B_1 equivalent surfaces for the surface coil and to achieve a uniform B_1 profile on the surfaces closest to the coil, different spacing (from 0 to 0.8 cm) above and beneath the coil was tested by calculating B_1 maps of the two agar phantoms. 0.5 cm above and below the surface coil was chosen to take into account both B_1 efficiency and B_1 homogeneity in the region of interest (ROI).

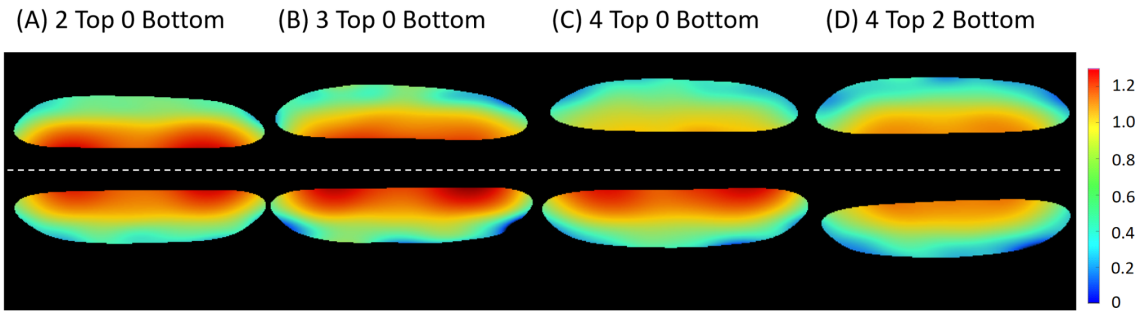

Figure 2.5: B_1 profiles of two identical 5% agar phantoms for symmetric B_1 testing. This experiment involved varying the number of fiberglass spacers, each 0.2 cm thick, on each side of the surface coil to achieve a uniform B_1 profile of 1 on each surface while avoiding inhomogeneities. Configurations from (A) to (D) demonstrate the effects of different spacer arrangements. The white dotted line marks the position of the surface coil. (A) shows symmetric B_1 distribution; however, it yields an average B_1 of 1.1 on both sides with higher B_1 values near the coil loop, indicating a lack of surface homogeneity. (B) and (C) show reduced B_1 values at the top with increased spacers on that side. (D) Achieves the targeted symmetric and uniform B_1 profile of 1 on both surfaces.

2.3.2 Agar T_2 Relaxation Measurement

Measuring the T_2 relaxation times in agar allows for a comparison with T2 relaxation in skin tissue. This comparison is particularly useful since skin is expected to exhibit a greater signal impact due to its much shorter expected T_{2fast} and T_{2slow} values compared to agar. The measurements were performed on a 5% agar phantom with a sodium concentration of 60 mM. T_2 measurements of agar were conducted using a sodium density-weighted sequence with the following parameters: TR=100 ms, flip angle=90^o, voxel size=1×1×5 mm^3, total acquisition time=2.5 minutes. The echo times used for the measurements were TE = [0.1, 0.8, 2.0, 3.5, 6.0, 9.0, 12.0, 16.0, 20.0, 25.0, 30.0] ms.

Signal intensities in each ROIs were acquired and subsequently subjected to biexponential fitting to distinguish between the fast and slow T_2 components. The signal intensities were fit to a 60%/40% T_{2fast}/T_{2slow} ratio. The analysis revealed that $T_{2fast(60\%)}$ = 4.3 ms, and the $T_{2slow\ (40\%)}$ = 27.2 ms.

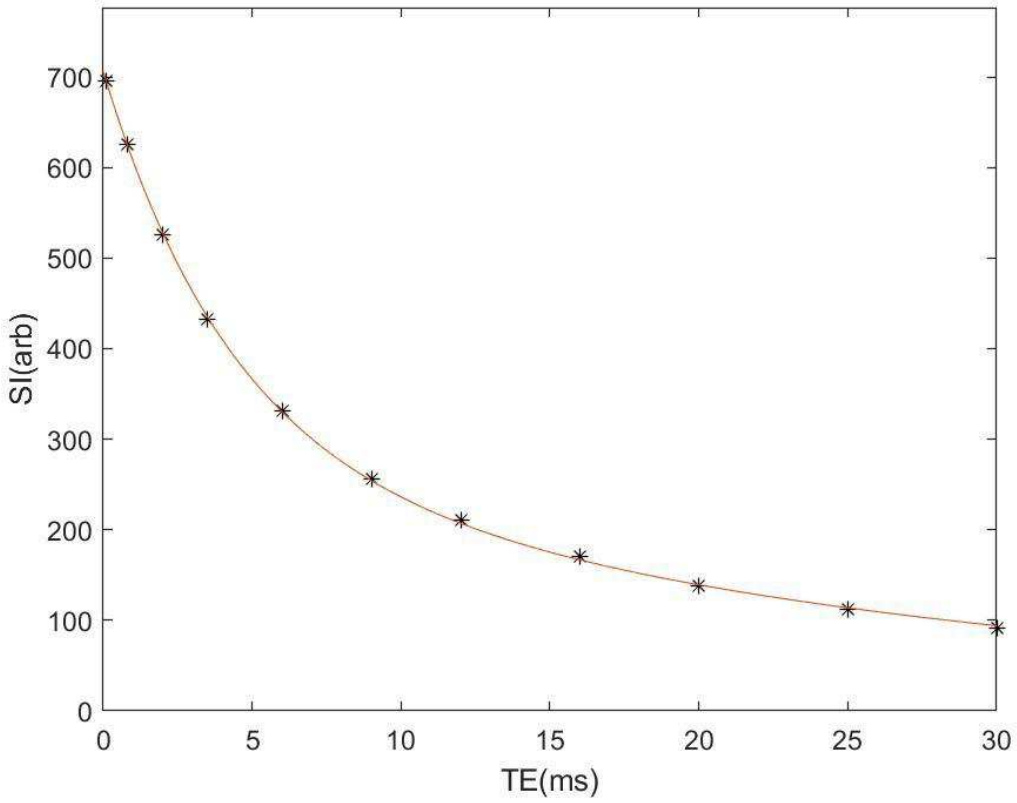

Figure 2.6: T_2 relaxation fitting of a 60 mM agar phantom used in this study. The graph shows signal intensity (SI) in arbitrary units plotted against echo time (TE) in milliseconds. Each data point (marked with an asterisk) represents the signal intensity at a specific TE, demonstrating a typical bi-exponential decay pattern as TE increases. The fitting yields $T_{2fast(60\%)} = 4.3$ ms and $T_{2slow\ (40\%)} = 27.2$ ms.

2.4 Sodium TPI Acquisition

2.4.1 Volunteer Study

Sodium images of the left calf were acquired on a Varian Inova 4.7T whole body scanner. Each participant underwent four ^{23}Na scans: one with volume coil and four with surface coil. The ^{23}Na MRI scans in this thesis each had 6000 TPI trajectories with each

trajectory duration=9 ms, TR=120 ms, ultra-short TE of approximately 0.1 ms enabled by TPI sequence, and a total scan duration of 12 minutes. The long TR of 120 ms was selected to allow full T_1 relaxation. At the beginning of each measurement, B_0 shimming and B_1 mapping were performed.

For volume coil imaging, one volume coil protocol with pencil-shaped voxels (*VolPencil*) was acquired with voxels of 1.5×1.5×15 mm^3. The imaging parameters were: TE=0.13 ms, TR=120 ms, and RF pulse duration=0.16 ms. The FOV was 16×16×16 cm^3. This protocol was designed to mimic the typical 'baseline' Kopp protocol which used a volume coil, 90° flip angle, and 3×3×30 mm^3 voxels. The efficient data acquisition in TPI enables the use of smaller voxel sizes within reasonable scan times without compromising the signal-to-noise ratio (SNR). B_1 maps for volume-coil imaging were created from two images with low resolution (6×6×12 mm^3) with prescribed flip angles of 60° and 120°, with a total scan time of 1.2 minutes.

The *SurfPencil* protocol employed pencil-shaped voxels that were five times smaller (0.8×0.8×10 mm^3) than those in the *VolPencil* protocol, with a 90° flip angle. The in-plane resolution of 0.8 mm was chosen because it is smaller than the average skin thickness in the calf of 1.1 mm to 1.5 mm[72,75,76]. This reduction in voxel size was enabled by the higher SNR efficiency of the surface coil. The SNR efficiency of an RF coil is approximately proportional to the square root of the volume it accommodates, making compact surface coils highly advantageous for skin imaging. The FOV for this protocol was 8×8×8 cm^3 to ensure complete coverage of the coil's sensitive area, with a TE of 0.12 ms and an RF pulse duration of 0.12 ms.

The *SurfPancake* protocol used pancake-like voxels ($0.4\times4\times4\ mm^3$) with a thinner dimension of 0.4 mm across the skin ($0.4\times4\ mm^2$ in-plane) and a 90° flip angle, with TE of 0.11 ms and an RF pulse duration of 0.12 ms. The $0.4\times4\ mm^2$ in-plane resolution was chosen to fit the anatomy of skin when the skin is pressed flat on the surface coil. The voxels are only 0.4 mm thin across the skin (~1.1-1.5 mm thick) which would further minimize partial volume effect compared with *VolPencil* protocol. Voxel reshaping was achieved by designing the trajectory in advance to sample a different matrix volume. The FOV for this protocol was restricted at $8\times8\times8\ cm^3$ to align with the limited sensitive area of the surface coil. Smaller FOV can also enable higher resolution given the same sampled data points. To investigate B_1, three *SurfPancake* images were acquired using the same RF power to generate flip angles of 60°, 90°, and 120° (RF pulse durations of 0.08 ms, 0.12 ms, and 0.16 ms, respectively). The 60° and 120° images were acquired for B_1 mapping.

2.4.2 Surface Coil Reproducibility Test

A reproducibility test was conducted to ensure that the results obtained from the surface coil MRI are reliable and consistently reproducible. Three subjects participated in the test: one female aged 23 and two males aged 28 and 29. The tests were carried out using the surface coil sodium MRI protocol specified in the study, with the *SurfPancake* protocol and a flip angle of 60 degrees. This protocol was chosen because it provides the highest uncorrected skin/agar sodium intensity.

Three MRI scans were performed using the protocol mentioned above, with a five-minute break given between each scan. During the break, the participant was removed from the

scanner and allowed to sit or walk before being repositioned in the scanner for the subsequent scan. Before the first scan, a reference line was drawn on the subject's calf and the line was maintained for all three scans. In each scan the line was aligned with the iso-center to ensure consistent imaging locations. Shimming was performed before each scan.

The variation in relative skin/agar (60 mM) sodium signal intensity within each subject was below 5%, indicating high consistency in the surface coil MRI results.

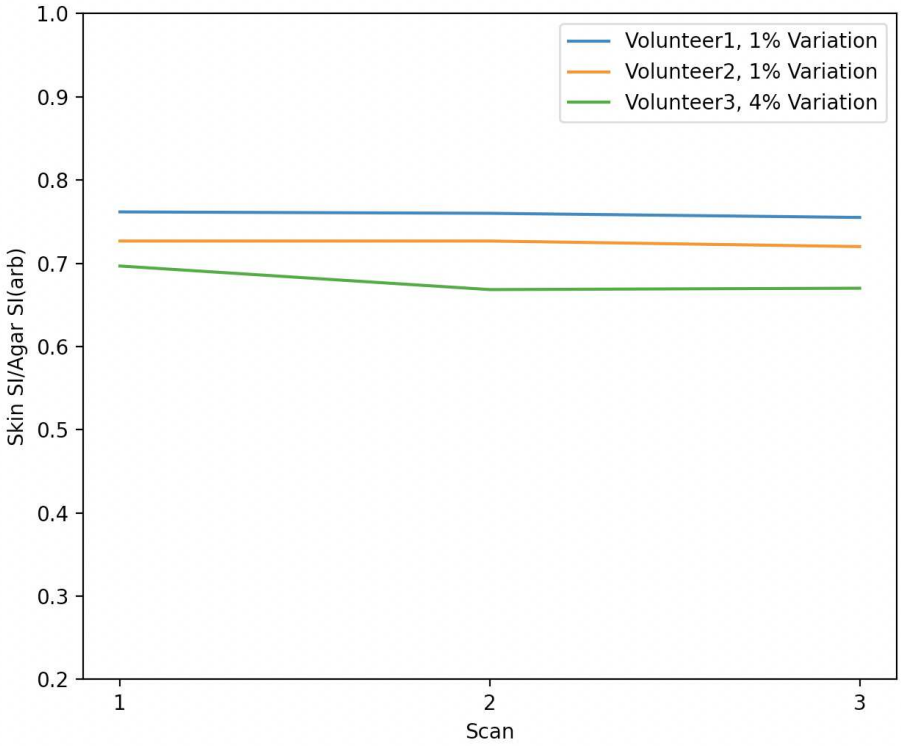

Figure 2.7: Variation in skin/agar signal intensity in arbitrary units across three scans for each volunteer. Skin/agar sodium signal intensity ratios are depicted for three volunteers, with Volunteers 1 and 2 exhibiting a 1% variation and Volunteer 3 a 4% variation, demonstrating high level of consistency.

2.5 Proton Imaging of Calf for Skin Thickness Measurement

An anatomical proton image was taken from each volunteer for anatomical reference and skin thickness measurement. The ^{1}H MRIs are acquired with the Siemens Prisma 3T scanner. A T_1 weighted fat-saturated GRE sequence was used to better separate ^{1}H signal from the skin and subcutaneous adipose tissue. The spatial resolution for this image was $0.31\times0.31\times5.0$ mm^3, and the in-plane resolution was interpolated to 0.156×0.156 mm^2. TE=3.0 ms, TR=7.4 ms, flip angle=6°, total acquisition time = 4 min.

To ensure precise anatomical alignment, a predefined reference line on each volunteer's calf was aligned with the isocenter using the scanner's localizing laser. A custom-made microfiber platform, identical to the one utilized in volume coil sodium imaging, was placed under the volunteer's calf. This platform was designed to press the skin flat, which aids in accurate skin thickness measurement. To prevent any movement during the scan, the calf and the platform were securely wrapped with a foam piece to avoid movement.

The ^{1}H anatomical image obtained was then used to measure the skin thickness. Image intensity values were interpolated along lines perpendicular to the surface at intervals of 0.039 mm (¼ of the pixel width). The skin thickness was measured by defining it as the width of the intensity profile at 60% of the maximum skin intensity.

2.6 TSC Quantification

2.6.1 ROI Analysis

A custom MATLAB software was developed in house at University of Alberta specifically for sodium MRI ROI analysis in this study. All sodium images were zero-filled to a 320 isotropic matrix to facilitate manual ROI analysis. This software facilitated the precise and consistent mapping of ROIs across all acquired images. All ROIs were manually drawn for each image to ensure accuracy.

For each ROI, a thin box was drawn in the first slice to define the initial boundary of the region. Subsequently, another thin box, ideally of identical size and in the same relative location to the iso-center as the first box, was drawn in the last slice of the ROI. The width and slice numbers of each ROI were kept consistent for all images.

In the case of volume coil imaging, the ROIs in agar phantoms were positioned close to the skin. For surface coil imaging, the ROIs in both skin and agar were positioned at the same distance from the surface coil. Representative ROIs are shown in **Figure 2.8**.

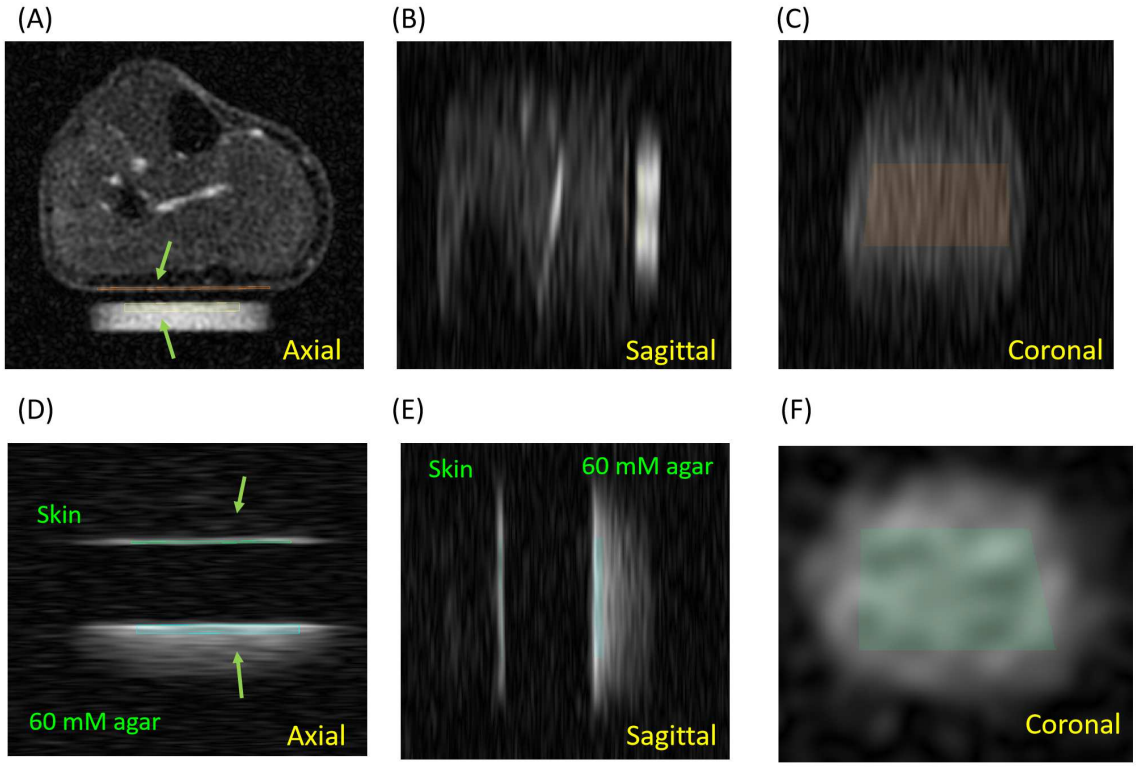

Figure 2.8: Representative ROIs for volume coil and surface coil imaging shown in the axial, sagittal and coronal planes. Arrows in **(A)&(D)** point to the ROIs in skin and agar respectively. **(A) (B) (C)**: ROIs are shown in axial, sagittal and coronal sodium MRI images acquired by volume coil. Sodium signal in the skin is noticeably higher than the sodium signal in subcutaneous fat tissue. There's also a noticeable amount of signal in muscle and blood veins. **(D) (E) (F):** ROIs in axial, sagittal, and coronal views acquired using a surface coil. The sodium signal in the skin is sharply distinguished from adjacent air and adipose tissue. However, sodium in deeper muscle tissues is not visible due to the surface coil's sensitivity to superficial layers.

2.6.2 B_1 Correction

TSC quantification without B_1 correction was initially achieved by comparing signal intensities in the skin and the agar phantom. However, B_1 correction is essential in this study to account for the spatial variation of coil's B_1 field, possibly due to calf skin having higher tissue conductivity and permittivity (**Figure 2.9**).

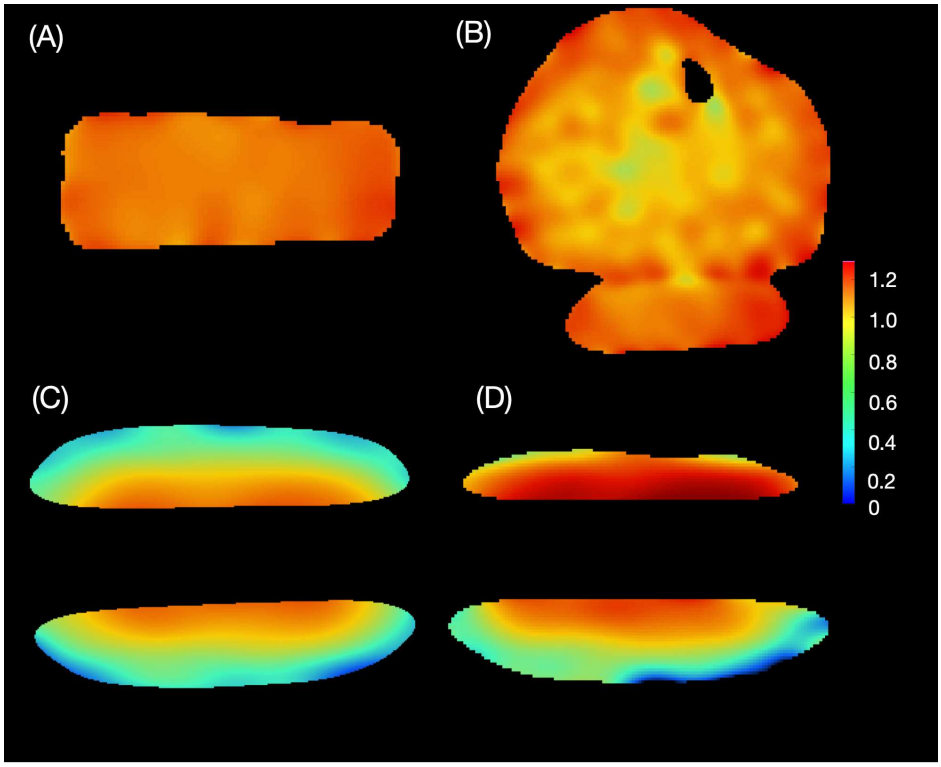

Figure 2.9: Low resolution volume coil B_1 map (**(A)&(B)**), surface coil B_1 map (**(C)&(D)**) from both phantom scans and volunteer scans, the variation in the B_1 map in the skin points to the necessity for B_1 correction in surface coil sodium MRI. **(A)** B_1 map from a volume coil scan of two identical 60 mM Na^+ agar phantoms (axial view), showing a relatively uniform relative B_1 field of 1. **(B)** B_1 map from a volume coil scan including the calf of a 46-year-old male and a calibration phantom, indicating similar B_1 values across the calf and phantom, both approximately 1. **(C)** B_1 map from a surface coil scan of two 60 mM Na^+ agar phantoms, depicting B_1 value at 1 at both surfaces near the coil, with 4 spacers above and 2 spacers below the coil described in **Figure 2.5**. **(D)** B_1 map from a surface coil scan of the same 46-year-old male's calf, where relative B_1 values are higher (~1.1) in the calf skin than in the phantom(~1).

The B_1 correction method implemented in this study is described as follows:

The B_1 field can exhibit spatial inhomogeneity, particularly when utilizing a surface RF coil. Surface coils demonstrate higher sensitivity near their surface, with sensitivity

rapidly decreasing as the distance from the surface increases. The rationale and steps for B_1 correction in this study are described as follows:

The actual flip angle (α_{actual}) at a point of tissue is defined as:

$$\alpha_{actual(r)} = \gamma B^{+}_{1(r)} \cdot \tau \quad (2.1)$$

Where $\alpha_{actual(r)}$ is the actual flip angle at a certain location of the tissue, γ is the gyromagnetic ratio of sodium, which is 11.26 MHz/T, $B^{+}_{1(r)}$ is the transmit RF field at the location of the tissue, and τ is the RF pulse duration.

The signal intensity at the tissue location r can be described as

$$SI(r) \sim \rho Na_{(r)} \cdot sin(\alpha_{actual(r)}) \cdot (w \cdot e^{-\frac{TE}{T_{2fast}}} + (1-w) \cdot e^{-\frac{TE}{T_{2slow}}}) \quad (2.2)$$

Where $SI(r)$ is the sodium MR signal intensity at location r, $\rho Na_{(r)}$ is the sodium density, w is the weight of T_{2fast} component, which is 0.6 in a homogeneous sodium environment and $(1-w)$ is the weight of T_{2slow} component, which would be 0.4 in a homogeneous sodium environment. TE is the echo time of the acquisition.

In this study, B_1^+ mapping was done using the double-angle method(as described in the introduction). B_1^- value was defined as the relative B_1 sensitivity rB_1.

The signal intensity correction with B_1^+ taken into consideration $SB^{+}_{1}corrected(r)$ would be:

$$S_{B_1^+ corrected}(r) = \frac{SI(r)}{sin(\alpha_{actual(r)})} \cdot sin(\theta) \quad (2.3)$$

Where $SI(r)$ is the acquired signal intensity at location r, and θ is the prescribed flip angle.

To perform signal intensity correction with both B_1^+ and B_1^- taken into consideration, the corrected signal intensity would be:

$$S_{corrected}(r) = \frac{S_{B_1^+ corrected}(r)}{rB_1} \quad (2.4)$$

Combining the two equations together, it follows that:

$$S_{corrected}(r) = \frac{SI(r) \cdot sin(\theta)}{sin(\alpha_{actual(r)}) \cdot rB_1} \quad (2.5)$$

Given that $\alpha_{actual} = rB_1 \cdot \theta$, the corrected signal intensity would be:

$$S_{corrected}(r) = \frac{SI(r) \cdot sin(\theta)}{sin(rB_1 \cdot \theta) \cdot rB_1} \quad (2.6)$$

2.7 Statistical Analysis

Paired t-tests were employed to evaluate the differences in skin TSC across all ^{23}Na MRI protocols obtained in this study. To investigate potential correlations between skin sodium concentration and other variables, multiple linear regression analyses were conducted. This approach allows for the examination of relationships between the

dependent variable(skin TSC) and multiple independent variables (skin thickness, age, and sex). The regression model for each ^{23}Na MRI protocol was formulated as:

$$TSC = \beta_0 + \beta_1 \cdot (skin\ thickness) + \beta_2(Age) + \beta_3(Sex) + \epsilon \qquad (2.7)$$

Where β_0 is the intercept, β_1,β_2 and β_3 are the coefficients for each independent variable, and ϵ is the error term. Given the limited sample size of 14 individuals, including only four older adults aged 46-61 years, the analysis of age and sex dependencies should only be considered preliminary.

Given the number of tests conducted, a correction for multiple comparisons was necessary to control the false discovery rate (FDR). The Bonferroni correction method was applied, setting the significance level at $p < \frac{0.05}{number\ of\ comparisons}$. All statistical analyses were performed using MATLAB.

3 Sodium MRI of the Skin Using a Surface Coil to Investigate and Reduce Signal Loss and Bias

A version of this chapter had been submitted for publication

(J. Zhu, C. Beaulieu, K. Damji, R. Stobbe)

3.1 Introduction

The measurement of skin sodium concentration is growing in interest with previous studies reporting elevated skin sodium levels in various pathologies including, but not limited to: hypertension[5], type 2 diabetes mellitus 11[12,49], chronic kidney disease with left ventricular hypertrophy[9], primary aldosteronism[8], acute kidney injury[57], and acute heart failure[48]. Additionally, greater skin sodium has been measured in males versus females 4[5,8] and in older individuals versus younger ones[5–7]. However, quantifying skin sodium concentration with ^{23}Na MRI is challenging. 'Gold standard' atomic absorption spectroscopy measured healthy skin sodium of ~77 mole/kg[8]. For a skin density of 1.1 kg/L[67], this amounts to a tissue sodium concentration of ~85 mM. The widely-adopted ^{23}Na MRI protocol of Kopp et al.[5,8,9,11,12,41,47–50,52,54,57–59,106] has measured healthy skin sodium concentration of only ~20 mM, across age and sex[5,8,12,48,52,57,106]. The purpose of this paper is to identify ^{23}Na MRI sources which contribute to this discrepancy, and to propose ^{23}Na MRI methodology that reduces sodium signal loss (bias).

The first problem of ^{23}Na MRI is that its concentration yields >1000× less signal than ^{1}H MRI, and for this reason, voxel volumes are necessarily large. The voxels of the widely-adopted Kopp protocol[8] are 3×3×30 mm³, however, the thickness of skin is only 1 to 2 mm[75,76]. Skin will only partially fill each 270 mm³ voxel, yielding signal biased by skin thickness and adjacent (^{23}Na sparse) adipose tissue. The problem is that skin thickness may vary with sex, age, ethnicity and pathology[72,107–111], thus yielding sodium concentration measurements biased by this variation. A primary goal of skin sodium MRI development must be to reduce voxel dimensions, particularly along the thickness of the skin. The widely adopted Kopp protocol has typically been implemented at 3T using a volume knee coil to image the skin of the calf[5,8,9,11,12,41,47–50,52,54,57–59,106]. While the use of a greater field strength magnet may be an option for some, the SNR efficiency of local surface coil imaging[112] is available for all field strengths. Only one paper has applied a surface coil to measure sodium concentration in calf, facilitating voxels of 0.9×0.9×30 mm^3 at 7.0T, and measuring greater sodium concentrations from 40 – 60 mM for men aged 20 – 80 years[7]. While this is clearly a large step in the right direction, voxel dimensions along the thickness of the skin should be reduced even further.

In addition to low sodium concentration, ^{23}Na exhibits very rapid (biexponential) signal decay in dense macromolecular environments[113]. Previous skin sodium relaxometry studies have reported $T_{2fast(14\%)}$=0.5 ms and $T_{2slow(86\%)}$=7.6 ms at 7T[7], as well as $T_{2fast(60\%)}$=0.4 ms and $T_{2slow(40\%)}$=9.3 ms at 4.7T[86]. However, the widely-adopted Kopp protocol[8] utilizes gradient-echo imaging with a lengthy TE~2 ms. Considerable signal

loss is expected, and any relaxation change with pathology could bias the tissue sodium concentration values measured.

The purpose of this work was to: (i) apply TPI[91] with TE ~ 0.1 ms to ^{23}Na MRI of the skin for the first time; (ii) investigate ^{23}Na MRI skin sodium measurement bias by skin thickness for volume coil imaging of the calf (voxels=1.5×1.5×15 mm^3); (iii) demonstrate increased signal (bias reduction) with SNR-efficient surface coil imaging, facilitating 5× smaller voxels (0.8×0.8×10 mm^3); and (iv) demonstrate further signal increase (bias reduction) with novel voxel reshaping to match the anatomy of pressed flat skin (0.4×4×4 mm^3).

3.2 Methods

A total of 14 healthy adults (aged 21 – 61 years, 8 male, 6 female) were recruited for this study and informed written consent was received for each participant. Skin sodium images from the left calf of each volunteer were acquired on a Varian Inova 4.7T whole-body scanner, but it should be noted that this ^{23}Na imaging protocol study is applicable to all magnetic field strengths and scanners. Sodium images were first acquired with a single-tuned birdcage ^{23}Na knee volume coil (diameter=17.8 cm, length=10 cm), as used in the Kopp protocol[8]. Volunteers were then removed from the scanner and the volume coil replaced with a transmit/receive sodium surface coil (diameter = 5 cm). The calf of each volunteer was marked with a line for magnet isocentre positioning, ensuring

the same skin tissue was assessed for both ^{23}Na volume coil, ^{23}Na surface coil, and ^{1}H images (below).

To measure skin thickness, ^{1}H T_1 weighted fat-saturated GRE images were acquired on a 3T Siemens Prisma with voxels = 0.31×0.31×5.0 mm^3 (interpolated to 0.156×0.156 mm^2 in-plane), TR = 7.4 ms, TE = 3.0 ms, flip angle = 6°, and scan duration = 4 min. Skin thickness measurement was enabled by resting the calf on a flat surface during ^{1}H imaging, as was done for ^{23}Na MRI (described below). At each pixel location along the flat skin, image intensity values were interpolated along lines perpendicular (@ pixel-width/4 = 0.039 mm) (**Figure 3.1A**). Averaging the interpolated values of each perpendicular line yielded a signal intensity profile across the skin (**Figure 3.1B**). For this study, skin thickness is represented by the profile width at 60% of the maximum skin intensity, a typical halfway value between relative adipose signal and maximum skin intensity. Note that while the absolute nature of these skin thickness measurements could not be anatomically confirmed, this method provided consistent analysis of skin thickness variation between volunteers.

TPI was used for all ^{23}Na MRI acquisitions, enabling TE ~ 0.1 ms, and for each ^{23}Na image, a total of 6000 TPI trajectories of 9 ms duration fully sampled k-space. A relatively long TR = 120 ms was selected to avoid T_1 weighting, yielding a scan duration of 12 minutes for each image. A 5% agar phantom with a sodium concentration of 60 mM was used for the purpose of ^{23}Na measurement calibration ($T_{2fast(60\%)}$ = 4.3 ms and $T_{2slow(40\%)}$ = 27 ms). The agar phantom filled a 90 mm diameter, 15 mm thick petri dish. For volume coil imaging, the calf was rested on a platform, and the agar phantom was

placed 0.3 cm below the calf. For surface coil imaging, the calf was rested on a platform 0.5 cm above the surface coil, while the same agar phantom was placed 0.5 cm below the surface coil. All images were reconstructed with standard gridding reconstruction, incorporating zero-filling to an isotropic matrix of 320×320×320.

Three ^{23}Na imaging methodologies were employed (detailed in **Table 3.1**). **(1)** The first ^{23}Na image was acquired with a volume RF coil, using 'pencil-shaped' voxels matching that of the Kopp protocol[5], although here the voxels were ~8 times smaller at 1.5×1.5×15=34 mm^3 (*VolPencil*). The fully-sampled FOV for this image was 16×16×16 cm^3. **(2)** The second ^{23}Na imaging methodology substituted the volume RF coil with the 5 cm diameter surface coil, while maintaining 'pencil-shaped' voxels (*SurfPencil*). Note, however, that voxel volume was reduced by 5× to 0.8×0.8×10=6.4 mm^3. This was facilitated by both the greater SNR-efficiency of surface coil imaging, and the smaller fully-sampled FOV = 8×8×8 cm^3 necessary to include all ^{23}Na nuclei excited by the 5 cm diameter surface coil. **(3)** The third ^{23}Na imaging methodology substituted the previous 'pencil-shaped' voxels with 'pancake-shaped' voxels having width = 0.4 mm across the skin for the same voxel volume = 0.4×4×4=6.4 mm^3 (*SurfPancake*). 'Pancake-shaped' voxels match the shape of skin (and beneficially fit within the skin) when the skin is pressed flat on a horizontal surface.

Sodium spin-density quantification with surface-coil imaging requires B_1 knowledge, both in the agar and skin. However, previous work showed that under the influence of very rapid signal decay, the generation of M_{xy} will deviate from that of sin(θ), where θ is the flip-angle[86]. To investigate B_1, two additional *SurfPancake* images were acquired

using the same RF power to generate flip-angles of 60° and 120° (i.e. RF pulse durations = 0.08 ms and 0.16 ms respectively). Region of interest (ROI) values in skin and agar (described below) for each of the 60°, 90°, and 120° images were fit to a $\sin(rB_1 \cdot \theta)$ dependence, where (rB_1) is relative B_1. As will be shown, agar was well fit by this standard excitation dependence, but the skin was not. Excitation was then simulated under the influence of rapid ^{23}Na biexponential relaxation using the tensor operators of Hancu[114]. Prescribed 60°, 90°, and 120° flip-angles (of the RF duration specified) were multiplied by rB_1= 0.6 to 1.4 (in 0.01 steps), and simulations performed for the resulting three flip-angles. The three measured (60°, 90°, and 120°) skin ROI values were then compared with the three simulated M_{xy} values at TE to determine the best fitting rB_1, using simple non-linear least square regression. Two measurements of ^{23}Na skin relaxation were considered for this fitting. The first included $T_{2fast(60\%)}$=0.4 ms and $T_{2slow(40\%)}$=9.3 ms derived from volume-coil imaging of the knee[86]. The second used the same relaxometry method, but in this case data acquisition was specifically focused on the skin with surface coil acquisition, yielding $T_{2fast(60\%)}$=0.17 ms and $T_{2slow(40\%)}$=12.5 ms[83]. Note that the relaxation measurement of Linz et al[7] at 7T cannot be simulated as it does not describe a homogeneous ^{23}Na environment with a 60%/40% T_{2fast}/T_{2slow} distribution. As will be shown, simulation using the second relaxation model with $T_{2fast(60\%)}$=0.17 ms fit the in vivo skin data the best. Sodium values in both skin and agar were then corrected by $\sin(rB_1 \cdot \theta)$ for B_1+ and by rB_1 for B_1-, using the rB_1 values from this fitting. For volume-coil imaging, B_1 maps were created from two low resolution (6×6×12 mm^3)

images with prescribed flip-angles of 60° and 120° using standard methodology. This protocol was chosen for the purpose of saving time, with a total scan time = 1.2 minutes.

Intentionally pressing flat the calf skin enabled a thin (2 zero-filled voxels) 0.5 × ~3.5 × ~3.5 mm^3 angled-box ROI to be centered within the skin for average ^{23}Na signal measurement. Average agar phantom signal was likewise measured with an angled-box ROI located at the top of the agar phantom, and similarly distanced from the coil as skin for surface coil imaging. Measured values are given in this study as the skin/agar ratio. These values could be multiplied by the 60 mM of the agar phantom and stated as TSC values, however, skin sodium concentration estimation will follow additional Discussion-based simulation and comparison with experiment. Paired t-tests were used to investigate differences between all ^{23}Na images. To test for correlation between skin sodium measurements and skin thickness, age and sex were also included in a multiple linear regression. This regression was performed for each of the protocols of **Table 3.1**, as well as for the 60° and 120° *SurfPancake* images used for B_1 analysis. Given 15 effective correlation tests over the five images, the multiple comparison corrected significance was set at $p < 0.003$.

Table 3.1: An overview of three ^{23}Na MRI protocols used for skin ^{23}Na investigation.

Protocol Name	***VolPencil***	***SurfPencil***	***SurfPancake***
Coil	Volume Coil	Surface Coil	Surface Coil
Total Scan Time	12 min	12 min	12 min
No. Trajectories	6000	6000	6000
Trajectory Duration	9 ms	9 ms	9 ms
FOV	16×16×16 cm^3	8×8×8 cm^3	8×8×8 cm^3
Voxel Size	1.5×1.5×15 mm^3	0.8×0.8×10 mm^3	0.4×4×4 mm^3
TR	120 ms	120 ms	120 ms
TE	0.13 ms	0.12 ms	0.11 ms
RF Pulse Duration	0.16 ms	0.12 ms	0.12 ms
Flip-angle	90^o	90^o	90^o

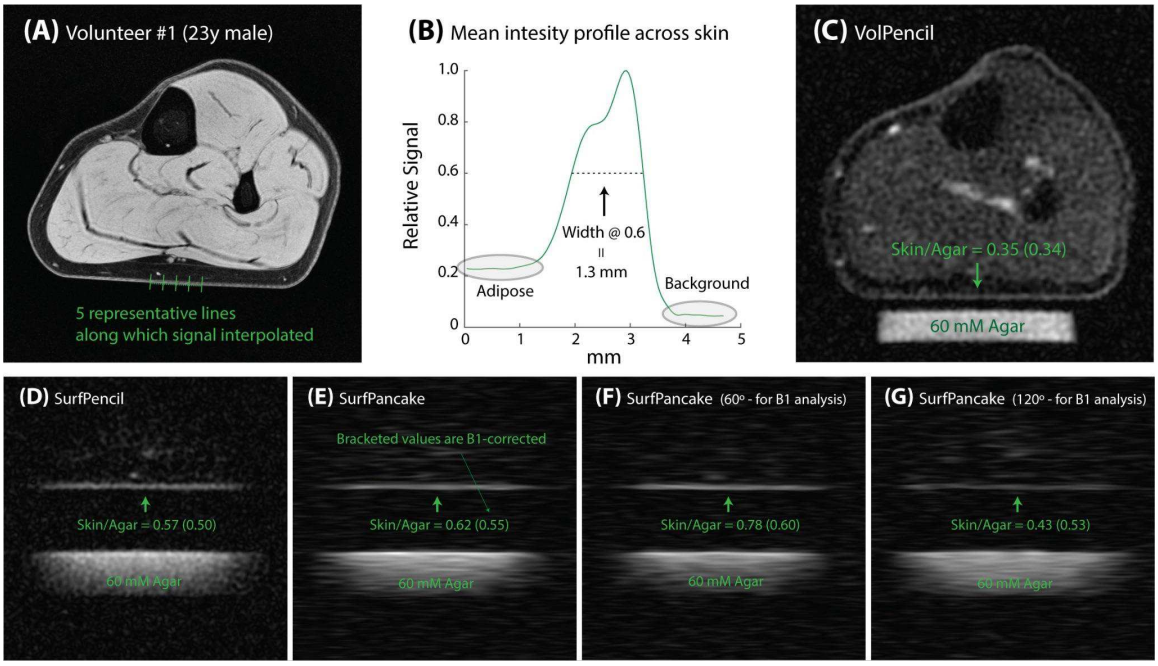

Figure 3.1: Representative images from Volunteer #1 (a 23-year-old healthy male). **(A)** ^{1}H signal was interpolated across lines perpendicular to the skin (one line per voxel along the skin). **(B)** The signal intensity along each line was then averaged to yield a mean intensity profile across the skin. For this study, the width of the intensity profile at 60% of the maximum value was chosen to represent skin thickness. Note that 60% is halfway between relative adipose signal and maximum intensity. For this volunteer, skin thickness was 1.3 mm. **(C)** Volume coil sodium images of the calf acquired with 1.5 mm 'pencil' voxels across the skin (*VolPencil*) yielded skin/agar = 0.35 (0.34) for this volunteer. Note that B_1-corrected ratios are given in brackets. **(D)** Surface coil imaging enabled smaller 0.8 mm 'pencil' voxels across the skin (*SurfPencil*), providing clearer depiction of the skin and yielding larger skin/agar = 0.56 (0.50). **(E)** 'Pancake' voxel reshaping for 0.4 mm thickness across the skin (*SurfPancake*) yielded even greater skin/agar = 0.62 (0.55). **(F,G)** The additional images used for B_1 analysis show elevated skin/agar for 60° flip-angles, and reduced skin/agar for 120° flip-angles. Note that the surface coil is located halfway between skin and agar.

3.3 Results

Figure 3.1 shows representative images from Volunteer #1 (a healthy 23-year-old male). For this individual, a skin thickness of 1.3 mm was measured from the bottom, pressed-flat region of the calf indicated (**Figure 3.1A-B**). The sodium image acquired with the knee volume coil and 'pencil-shaped' 1.5×1.5×15=34 mm^3 voxels (*VolPencil* – **Figure 3.1C**) yielded SNR = 10.9 and a skin/agar sodium image intensity ratio = 0.35 (0.34). Note that the bracketed values are B_1-corrected (discussed below). The switch to surface coil imaging (*SurfPencil* – **Figure 3.1D**) facilitated approximately 5× smaller voxels (0.8×0.8×10=6.4 mm^3) for similar SNR = 12, and yielded considerably greater skin/agar = 0.57 (0.50). Subsequent voxel reshaping to 0.4×4×4=6.4 mm^3 (*SurfPancake* – **Figure 3.1E**) produced even greater skin/agar = 0.62 (0.55). **Table 3.2** presents the skin/agar ratios obtained from the three different ^{23}Na protocols for all 14 participants, along with skin thickness. For each individual, greater skin/agar is obtained with each protocol modification from **Figure 3.1C** to **3.1E**.

Surface coil B_1 analysis was facilitated by the additional acquisition of 60° and 120° flip-angle images with the same *SurfPancake* protocol shown in **Figure 3.1E** (which used 90° flip-angle excitation). The skin/agar sodium image intensity ratio = 0.78 for the 60° image (**Figure 3.1F**) is considerably greater than skin/agar = 0.62 for the 90° image (**Figure 3.1E**), which in turn is much greater than skin/agar = 0.43 for the 120° image (**Figure 3.1G**). Mean (uncorrected) values for each flip-angle image (across all 14 volunteers) are shown in **Figure 3.3A**. This points to considerably greater rB_1 in skin compared to agar, even though the surface coil was centered between the skin and the

agar. Note that if the relative B_1s are the same in skin and agar, the skin/agar ratio should remain constant, regardless of prescribed flip-angle. Fitting the agar ROI measurements of the $\theta = 60^o$, 90^o and 120^o images with a $\sin(rB_1 \cdot \theta)$ dependence yielded an average $rB_1 = 1.02 \pm 0.09$ (standard deviation) in agar across individuals (**Figure 3.2**). The same fitting yielded a much larger average skin $rB_1 = 1.25 \pm 0.09$, but a $\sin(rB_1 \cdot \theta)$ dependence does not fit the skin ROI measurements well. The data values from the 60^o and 120^o images are significantly 'too high', while those from the 90^o images are significantly 'too low' ($p = 0.0002$ for each). Simulated excitation under the influence of skin sodium relaxation of $T_{2fast(60\%)} = 0.17$ ms & $T_{2slow(40\%)} = 12.5$ ms[83] yielded the best fitting and $rB_1 = 1.21 \pm 0.08$ across individuals. Although there is considerable heterogeneity in the rB_1 of skin and agar, the difference between the skin and agar values is quite consistent for each individual; rB_1 was 19%±3% greater in skin than agar. Both skin and agar signal measurements were divided by $\sin(rB_1 \cdot \theta)$ for B_1+ correction, and by rB_1 for B_1- correction, using individual rB_1 measurements from the best simulation fitting. Note that the rB_1 attained from the best fitting simulation is only 3% less than that attained with simple $\sin(rB_1 \cdot \theta)$ fitting, and thus the B_1 correction difference between these two rB_1 values will be small, however, best data fitting to the simulation which includes the skin sodium relaxation of $T_{2fast(60\%)} = 0.17$ ms & $T_{2slow(40\%)} = 12.5$ ms[83] points to the validity of this relaxation for use in further skin imaging analysis.

Mean B_1-corrected skin/agar sodium image intensity was 0.34±0.07 for the *VolPencil* protocol, 0.48±0.08 for *SurfPencil*, and 0.57±0.09 for *SurfPancake*, each significantly different ($p < 1e^{-8}$) (**Figure 3.3B**). Although there is considerable skin/agar heterogeneity

across volunteers, each participant demonstrates progressive skin/agar increase from *VolPencil* to *SurfPencil* (44%±16% mean ± std increase) to *SurfPancake* (additional 20%±9%). Following B_1-correction, the 60° *SurfPancake* image yielded 6.6%±2.7% greater skin/agar than the 90° image, while the 120° *SurfPancake* image yielded 6.2%±2.5% less skin/agar than the 90° image ($p < 1e^{-4}$). These differences between the B_1-corrected images with different flip-angles will be addressed in the Discussion.

Table 3.2 lists skin thickness for each volunteer, with an average study thickness of 1.34 ± 0.25 mm (mean ± std). Sodium concentration bias by skin thickness is a primary concern, given ^{23}Na imaging voxel size, and in **Figure 3.4**, skin/agar values are plotted with respect to skin thickness. For the 1.5×1.5×15=34 mm^3 voxels of *VolPencil*, skin/agar visibly increases with skin thickness (**Figure 3.4A**), and multiple linear regression testing (additionally accounting for age and sex) yields significant correlation between skin thickness and skin/agar measurement at an estimated rate (and standard error) of 0.19±0.05 /mm (at multiple comparison corrected $p < 0.003$). This amounts to a 56% increase from the skin thickness of 1 mm to 1.8 mm (the approximate range measured in this paper). Measured skin sodium is also visibly dependent on skin thickness for the 5× smaller (0.8×0.8×10=6.4 mm^3) pencil voxels of *SurfPencil* (**Figure 3.4B**), yielding significant correlation at 0.22±0.05 /mm ($p < 0.003$), or a 44% increase from 1 mm to 1.8 mm skin thickness. However, when voxels are altered to a pancake-like shape matching skin (0.4×4×4=6.4 mm^3), skin/agar no longer significantly correlates with skin thickness. This is true for each *SurfPancake* image regardless of flip-angle (**Figure 3.4C-E**). Multiple linear regression did not yield a significant skin/agar correlation with sex or age

(at multiple comparison corrected $p < 0.003$). However, across all 5 protocols, a skin/agar correlation with age is strongly *suggested*, even though the number of older volunteers is small.

Example images in **Figure 3.5** highlight skin/agar sodium intensity differences between thicker (1.5 mm) and thinner (1.0 mm) skin for two similarly aged females. For the *VolPencil* protocol, the thicker skin yields 44% greater B_1-corrected skin/agar. However, the relative difference is much smaller for the *SurfPancake* (90^o) protocol where B_1-corrected skin/agar = 0.52 for the thicker skin is only 16% greater than skin/agar = 0.45 for the thinner skin. This points to reduced ^{23}Na measurement bias by skin thickness for surface coil imaging with voxels reshaped for a small (0.4 mm) dimension across the skin.

Table 3.2: Skin thickness and skin/agar ratios for all volunteers.

Volunteer#	*Sex*	*Age (years)*	*Skin Thickness (mm)*	*Skin/Agar (B_1-Corrected in Brackets)*			*Relative Surface Coil B_1 Skin (Agar)*
				VolPencil	*SurfPencil*	*SurfPancake*	
1	Male	23	1.30	0.35 (0.34)	0.57 (0.50)	0.62 (0.55)	1.20 (1.01)
2	Male	27	1.10	0.25 (0.25)	0.43 (0.40)	0.54 (0.50)	1.27 (1.08)
3	Male	27	1.20	0.32 (0.32)	0.53 (0.46)	0.66 (0.57)	1.14 (0.96)
4	Male	27	1.22	0.31 (0.30)	0.62 (0.49)	0.69 (0.55)	1.04 (0.85)
5	Male	22	1.56	0.29 (0.28)	0.53 (0.46)	0.57 (0.49)	1.18 (0.98)
6	Female	23	0.98	0.25 (0.25)	0.38 (0.33)	0.53 (0.45)	1.18 (0.98)
7	Female	26	1.26	0.34 (0.33)	0.47 (0.41)	0.57 (0.50)	1.21 (1.00)
8	Female	23	1.53	0.34 (0.33)	0.50 (0.48)	0.58 (0.56)	1.33 (1.15)
9	Female	23	1.22	0.30 (0.29)	0.48 (0.49)	0.61 (0.62)	1.40 (1.23)
10	Female	24	1.46	0.37 (0.36)	0.51 (0.45)	0.58 (0.52)	1.18 (1.01)
11	Male	46	1.81	0.51 (0.51)	0.78 (0.67)	0.90 (0.78)	1.18 (0.98)
12	Male	61	1.44	0.49 (0.48)	0.63 (0.57)	0.76 (0.70)	1.24 (1.06)
13	Male	53	1.68	0.43 (0.40)	0.68 (0.57)	0.79 (0.66)	1.15 (0.95)
14	Female	56	0.96	0.30 (0.29)	0.46 (0.42)	0.61 (0.57)	1.24 (1.07)

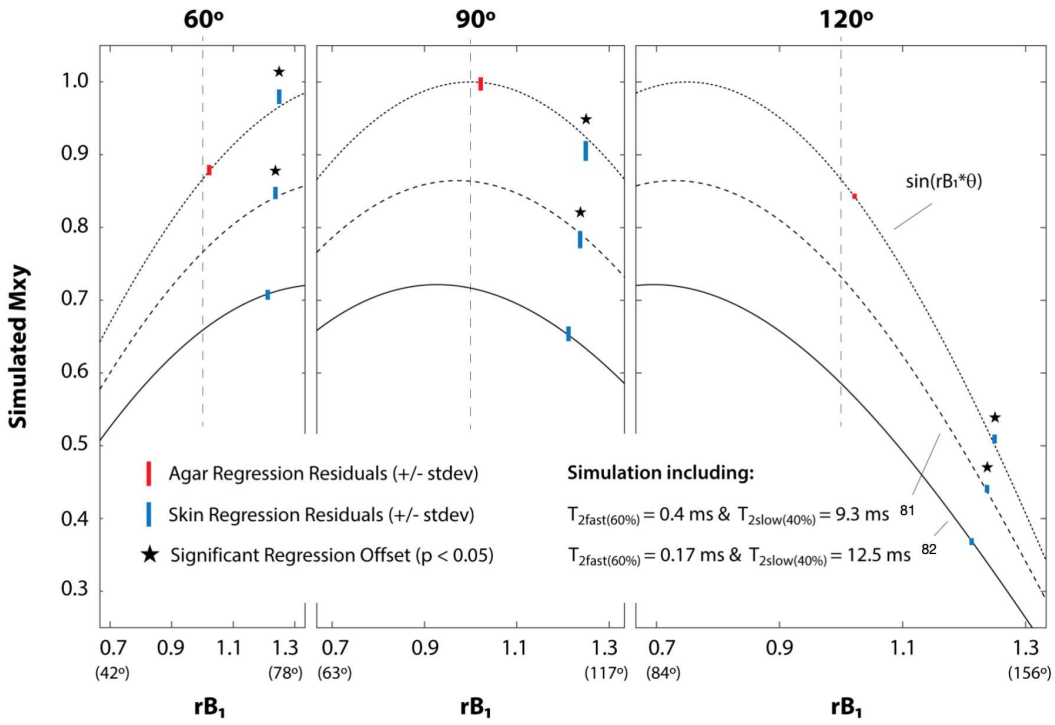

Figure 3.2: Simulated M_{xy} is plotted following prescribed flip-angles of 60°, 90° and 120°, where the actual flip-angle = $rB_1 \cdot \theta$. The dotted line is the ideal excitation case of $M_{xy}=\sin(rB_1 \cdot \theta)$. The dashed line includes excitation simulation under the influence of $T_{2fast(60\%)}$ = 0.4 ms and $T_{2slow(40\%)}$ = 9.3 ms[86], while the solid line includes simulation with $T_{2fast(60\%)}$ = 0.17 ms and $T_{2slow(40\%)}$ = 12.5 ms[83]. Note that the scaling of the plots along the x-axis reflects the actual flip-angle range (in brackets) associated with rB_1 for each prescribed flip-angle. The locations on each plot where rB_1=1.0 are indicated with a vertical line. Mean residuals (across individuals) from agar ROI fitting to $\sin(rB_1 \cdot \theta)$ are shown in red (± stdev), and are plotted with respect to $\sin(rB_1 \cdot \theta)$ at the mean rB_1=1.02 locations. The mean residuals from the agar fitting are not significantly different than zero, and thus straddle the $\sin(rB_1 \cdot \theta)$ curve. However, skin (blue) ROI fitting to $\sin(rB_1 \cdot \theta)$ yields systematic regression offsets, i.e. the regression residuals are significantly different than zero (p = 0.0002 for all). Skin ROI data better fits the simulation which includes T_{2fast} = 0.4 ms[86], but the residuals are still significantly (and systematically) different than zero (p = 0.02 for all). Finally, skin ROI data best fits the simulation which includes T_{2fast} = 0.17 ms[83]. Here regression residuals are not significantly different than zero and thus straddle the simulation line. This best fitting case yielded an average rB_1 = 1.21 ± 0.08, a value 19%±3% greater than the rB_1 = 1.02 ± 0.09 in agar.

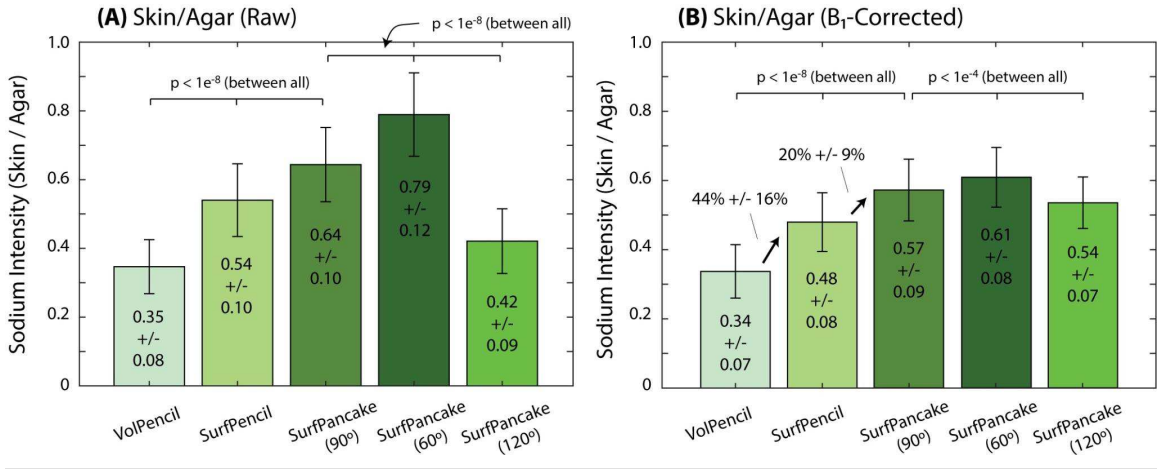

Figure 3.3: **(A)** Raw (uncorrected) skin/agar sodium image intensity values. **(B)** Following B_1 correction, the 0.8×0.8×10=6.4 mm^3 voxels of the *SurfPencil* protocol yield 44%±16% greater skin/agar than the 5× larger 1.5×1.5×15=34 mm^3 voxels of *VolPencil*. Pancake voxel reshaping to 0.4×4×4=6.4 mm^3 yields an additional 20%±9% greater skin/agar for *SurfPancake* (90°) compared to *SurfPencil*. The B_1 corrected values of the *SurfPancake* 60°, 90° and 120° images exhibit a near linear decrease with flip-angle. The skin/agar value of *SurfPancake* (90°) is 6%±2% less than *SurfPancake* (60°), while the skin/agar value of *SurfPancake* (120°) is 6%±2% less than *SurfPancake* (90°).

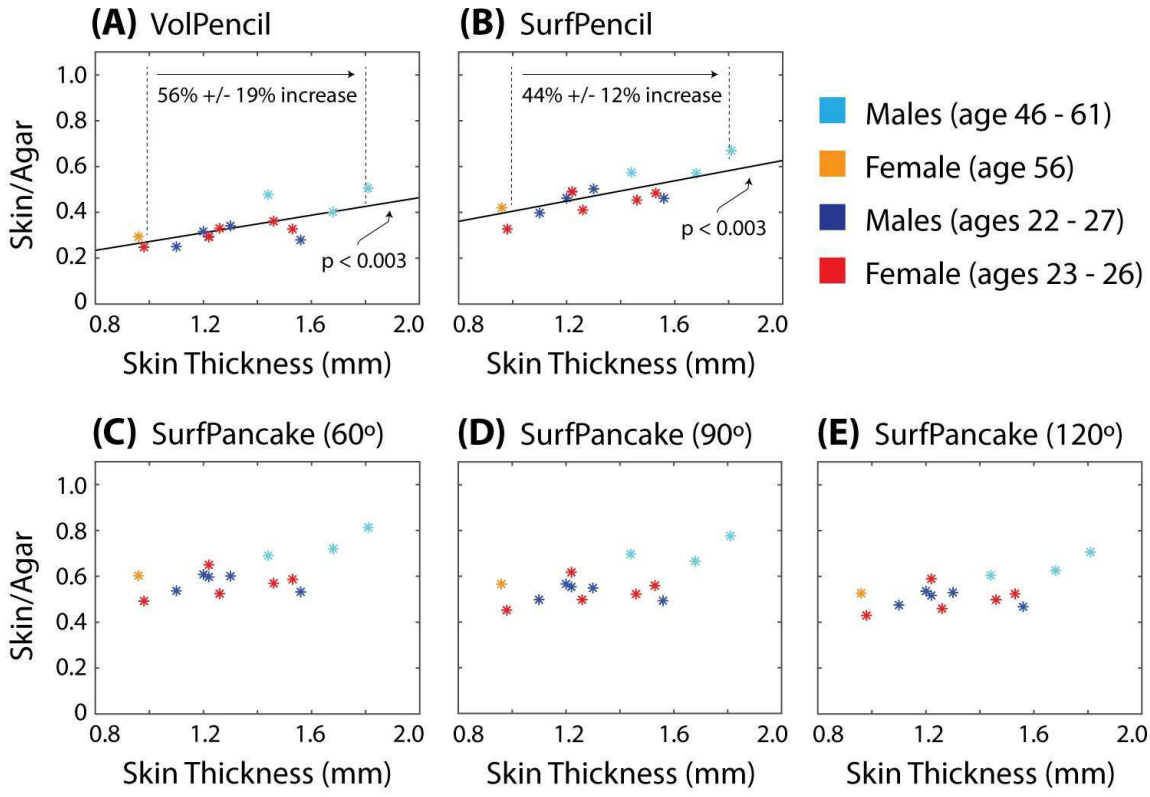

Figure 3.4: **(A)** Skin/agar sodium image intensity correlates with skin thickness for the volume-coil (*VolPencil*) protocol with 1.5×1.5×15=34 mm^3 voxels, when age and sex are also taken into account within a multiple linear regression ($p < 0.003$, for multiple comparison correction). The linear relationship of this regression yields a 56%±19% (standard error) increase over the range of skin thicknesses measured in this study (~1.0–1.8 mm). **(B)** The smaller 0.8×0.8×10=6.4 mm^3 voxels of the *SurfPencil* protocol also yield significant correlation between skin/agar and skin thickness, but at a smaller 44%±12% image intensity increase from 1.0–1.8 mm. **(C-E)** The shift to 0.4×4×4=6.4 mm^3 pancake-shaped voxels results in loss of significant correlation between skin/agar image intensity and skin thickness. While a skin/agar correlation with skin thickness appears evident in (**C-E**), multiple linear regression also suggests strong skin/agar dependence on age, although, with only 4 older volunteers, this is not significant at $p < 0.003$. Visual analysis of just the younger volunteers also suggests minimal skin/agar correlation with skin thickness in (**C-E**).

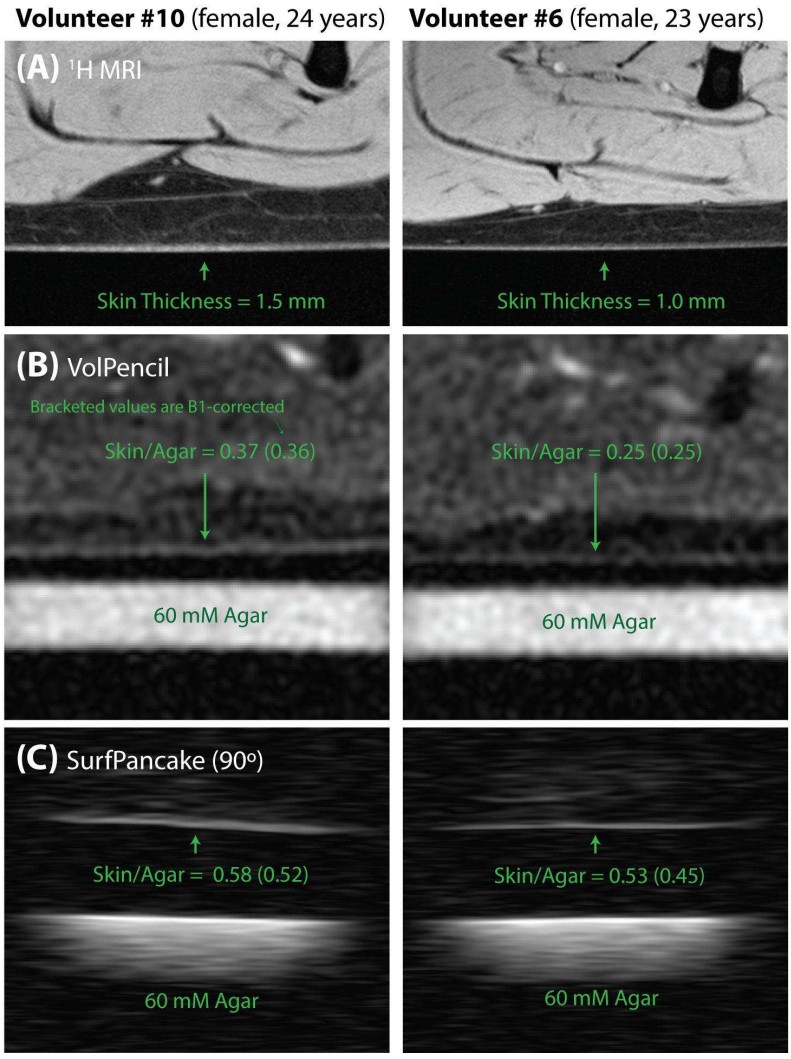

Figure 3.5: (A) ^{1}H images from two similarly aged young adult females demonstrate visibly different skin thickness (i.e. the skin thickness of volunteer #10 is 50% greater than that of volunteer #6). **(B)** The *VolPencil* sodium image from volunteer #10 with thicker skin yields 44% greater B_1 corrected Skin/Agar sodium signal = 0.36 than the image from volunteer #6 which yields Skin/Agar = 0.25. **(C)** However, when the *SurfCoilPan90* protocol is used, the B_1 corrected Skin/Agar = 0.52 from volunteer #10 is only 16% greater than the B_1 corrected Skin/Agar = 0.45 from volunteer #6. Reduced relative Skin/Agar difference between volunteers with different skin thickness for the pancake shaped voxels points to reduced bias by skin thickness. Note that the spatial scale is the same for each image.

3.4 Discussion

Surface-coil imaging with (0.4×4.0×4.0=6.4 mm^3) pancake-shaped voxels (*SurfPancake*) yielded the greatest B_1-corrected skin/agar sodium image intensity, with mean values 68% greater than volume-coil imaging with (1.5×1.5×15=34 mm^3) voxels (**Figure 3.3B**). This increase points to a reduction in signal loss (bias) for thin skin imaging with 0.4 mm thick voxels across the skin. Multiplying the mean skin/agar sodium intensity = 0.57±0.09 for *SurfPancake* (90°) with the agar concentration of 60 mM yields an apparent TSC of 34.2±5.4 mM. This is greater than previous measurements of ~20 mM using the standard gradient-echo method with 3×3×30 mm^3 voxels and TE ~ 2 ms[5,8,12,48,52,57,106], but it is still substantially less than the ~85 mM expected from atomic absorption spectroscopy (~77 mmole/kg)[8] and skin density (1.1 kg/L)[67]. While previous TSC calculations have been based on negligible relaxation effect between skin and agar at TE ~ 2 ms[8], here, the skin relaxation of $T_{2fast(60\%)}$ = 0.17 ms and $T_{2slow(40\%)}$ = 12.5 ms[83] that best fit surface-coil B_1 experiment is expected to have much greater signal impact than the agar relaxation of $T_{2fast(60\%)}$ = 4.3 ms and $T_{2slow(40\%)}$ = 27 ms, even for the short TE ~ 0.1 ms of TPI. It is for this reason that simple TSC calculations were not presented in the Results and Figures. Here, the effect of rapid biexponential ^{23}Na relaxation is investigated for the images of this study, alternative skin sodium MRI methods proposed, and 'relaxation compensated' TSC estimates generated.

Figure 3.6A demonstrates the simulated creation of M_{xy} during an RF pulse under the influence of the skin sodium relaxation described above. For smaller ω_1 (i.e. longer RF pulses), the shape of RF excitation is shifted away from that of a sinusoid. The maximum

M_{xy} generated is reduced from 1.0, and the maximum location is shifted to flip-angles less than 90°. Note that it is the altered excitation shape of the ω_1 = 2500 Hz excitation profile that best fits the image intensities of the (prescribed) 60°, 90° and 120° *SurfPancake* images in **Figure 3.4**. For small flip-angles, M_{xy} is very similar to that of $sin(\theta)$, but as the RF pulse progresses, the relative difference between M_{xy} and increases. **Figure 3.6B** demonstrates that the M_{xy} decrease from $sin(\theta)$ during the RF pulse is approximately linear in this case. From this figure, M_{xy} following the 73° flip-angle in skin of the *SurfPancake* (60°) protocol (including the average = 1.21 in skin) is 87% of , i.e. a 13% signal loss compared to environments like agar that yield M_{xy} according to . M_{xy} following the 109° flip-angle of the *SurfPancake* (90°) protocol is 82% of (an 18% signal loss), and M_{xy} following the 145° flip-angle of the *SurfPancake* (120°) protocol is 77% of . This flip-angle dependent signal loss matches that of the B_1-corrected *SurfPancake* images in **Figure 3.3B**. The (prescribed) 90° images yield a mean skin/agar value 6%±2% less than the 60° images, while the 120° images yield a mean skin/agar 6%±2% less than the 90° images. This decrease can also be seen across individual volunteers in **Figure 3.4C-E**.

In **Figure 3.6A-B**, larger flip-angles are inherently associated with longer RF pulse duration, and hence TE. Calculating signal loss at the end of the RF pulse according to

$$M_{xy}(\tau_{RF}/2) = 0.6exp(-\frac{\tau_{RF}/2}{T_{2fast}}) + 0.4(-\frac{\tau_{RF}/2}{T_{2slow}}) \quad [3.1]$$

where τ_{RF} is the duration of the RF pulse, results in $M_{xy}(\tau_{RF}/2)$ = 0.87, 0.82 and 0.77 respectively for τ_{RF} = 0.08 ms (60°), 0.12 ms (90°), 0.16 ms (120°). These are the same relative M_{xy} values given above and in **Figure 3.6B**. Thus, the standard calculation of **Eq. 3.1** is sufficient to describe signal loss at the end of the RF pulse, and the trends of **Figure 3.6A-B**. However, it should be noted that the M_{xy} produced at the end of the RF pulse will still decay according to **Eq. 3.1** after the RF pulse. In other words, the signal loss during the RF pulse "reduces both the fast and slow decaying components of M_{xy} equally". This is demonstrated in **Figure 3.6C** with continued simulation following the RF pulse. Thus, to calculate signal loss at TE, where TE =$\tau_{RF}/2 + T_D$ (and T_D is a delay following the RF pulse), one must first calculate $M_{xy}(\tau_{RF}/2)$ and then $M_{xy}(T_D)$ from the end of the pulse. This is a unique requirement for the inherent biexponential relaxation of spin 3/2 (i.e. it is not necessary for monoexponential relaxation). Even if TE is held constant at a relatively long value (for example, 2 ms) the duration of the RF pulse (which may be much smaller than TE) may still substantially impact the value of M_{xy} at TE. RF pulse durations should be reported for ^{23}Na studies. Depending on RF pulse duration, the M_{xy} at TE = 2 ms (which is commonly used by previous studies[5,8,9,11,12,41,47–50,52,54,57–59,106]) may only be 25% of M_o (**Figure 3.6C**), or less (for even longer RF pulses). Following a delay of 46 μs, the *VolPencil* and *SurfPancake* (90°) protocols yield M_{xy} values 66% and 70% of M_o (**Figure 3.6C**). One approach to minimize signal loss during RF excitation is to implement even shorter, higher power RF pulses. In this study, RF power for surface-coil imaging was not constrained by SAR, but by surface-coil hardware limitation. Alternatively, smaller flip-angles also yield shorter RF pulses and less signal

loss. Techniques like single-point-imaging have used very small flip-angles for quantitative ^{23}Na imaging in the past[115], the drawback being less absolute signal and SNR. Finally, for completeness, it should be noted that tensor operator simulation does indicate that a small T_{31} magnetic moment is present by the end of the RF pulse[114], which will slightly alter M_{xy} decay following the RF pulse, but this effect is small (in this context), decreasing the fast decaying fraction to 59% for *SurfPancake* (60°), and increasing it to 61% for *SurfPancake* (90°) and 62% for *SurfPancake* (120°).

To investigate the skin/agar sodium intensity dependence on skin thickness, simulated imaging was performed using the relative M_{xy} values of the protocol readouts given in **Figure 3.6C**. Numerical boxes with width = 3,4,5,6,7,8 voxels were created within the context of a 320×320×320 matrix for surface coil imaging and a 640×640×640 matrix for volume coil imaging, yielding widths = 0.75,1.0,1.25,1.5,1.75,2.0 mm for the associated FOVs of 80 mm and 160 mm, respectively. Lengths in the other two dimensions were 60 mm in each case. The k-space of these six simulated skin boxes was sampled (using the methodology of[116]) and multiplied by the relative M_{xy} of **Figure 3.6C**. Images were created with standard gridding reconstruction. Note that the image intensity = 1.0 (at the centre of sufficiently thick simulated skin) when k-space is not multiplied by the relative M_{xy} of **Figure 3.6C**. Reduction from 1.0 is a result of both reduced M_{xy} at the centre of k-space and PSF related signal smearing beyond the boundaries of the skin. Both the *VolPencil* and *SurfPencil* protocols demonstrate clear image intensity increase with simulated skin thickness **(Figure 3.7A,B)**. However, the *SurfPancake* protocol exhibits an

image intensity that appears constant over skin thicknesses from 1.0 mm to 2.0 mm, at a relative image intensity value of approximately 0.35 (**Figure 3.7C**).

Simulated skin image intensity values are plotted in **Figure 3.8**, where values were measured using the same ROI analysis as the in vivo skin experiment. In **Figure 3.8A**, these values are interpolated at the mean skin thickness = 1.34 mm measured in this study. At this thickness, simulated skin image intensities were 0.19, 0.30 and 0.36 respectively for the *VolPencil*, *SurfPencil*, and *SurfPancake* (90^{o}) images. This amounts to a 55% image intensity increase from *VolPencil* to *SurfPencil*, and a 20% increase from *SurfPencil* to *SurfPancake*. These increases are similar to the 44%±16% and 20%±9% increases measured experimentally across all 14 volunteers (**Figure 3.3B**). **Figure 3.8B** shows that across the skin thickness range measured in this study (1 mm to 1.8 mm), the simulated image intensity of the *VolPencil* protocol increases 65% in a near linear fashion. *SurfPencil* increases 38% over this range, while *SurfPancake* increases only 5%. These image intensity increases with skin thickness are similar to those associated with multiple linear regression in **Figure 3.4**, i.e. 56%±19% for *VolPencil* and 44%±12% for *SurfPencil*, and no significant increase for *SurfPancake*. Similarities between simulation and experiment suggest that simulation may be a useful tool to explain ^{23}Na signal loss in skin. Small differences between simulation and experiment may be associated with skin thickness measurement error, varying ^{23}Na relaxation between individuals, and partial volume averaging of skin with adjacent ^{23}Na signal from adipose tissue (including signal from blood vessels etc) in vivo.

Even though there are five 0.4×4×4 voxels across 2 mm thick skin for the *SurfPancake* (90°) protocol, the relative image intensity at the centre of 2 mm thick skin is only 0.37 (**Figure 3.8C**). Given that M_{xy} = 0.70 at the centre of k-space (**Figure 3.6C**), this amounts to an additional 53% image intensity loss associated with PSF smearing. Very rapid signal decay around the centre of k-space will spread the signal associated with T_{2fast} well beyond this skin. Thus the short TE ~ 0.1 ms of TPI does not provide the reduced signal loss advantage one might expect from short TE in this context of ^{23}Na skin imaging. Minimizing PSF smearing for very rapid T_{2fast} may require techniques that employ single-point imaging around the centre of k-space with very short delay following excitation for each point[117]. Although signal is weighted lower by rapid T_{2fast} decay, the 0.4×4×4 voxels of the *SurfPancake* protocol yield the advantage of near constant weighting over the skin thickness measured in this study (1 mm to 2 mm in the simulation of **Figure 3.8B**). Very large voxels of other volume-coil gradient-echo methods (i.e. 3×3×30 mm^3 [8]) would be expected to yield signal bias directly related to skin thickness, i.e. 1.8 mm thick skin would fill 80% more of a voxel that 1 mm thick skin, and thus the voxel will have 80% greater intensity for 1.8 mm thick skin. Pathologies yielding edema[42,118,119] are a particular concern. Recent ultrasound study measured a skin thickness increase from 1.4 mm to 2.2 mm in healthy volunteers with histamine induced edema[120]. For large voxel ^{23}Na MRI, skin thickness change resulting from edema would be reflected as a TSC increase. Thus, surface coil imaging for greater SNR efficiency (as suggested by[7]), and voxel shaping to match pressed flat skin with

small voxel dimensions across the skin, yields a valuable approach to ^{23}Na imaging of skin for reduced TSC measurement bias by skin thickness.

Given the good correspondence between experiment and simulation in this study, the simulated relative sodium intensity values at the mean skin thickness = 1.34 mm in **Figure 3.8A** were used to estimate skin TSC = 93±15 mM from the mean skin/agar sodium intensity values of the *SurfPancake* protocol in **Figure 3.3B**, a value in the range of the 85±18 mM from absorption spectrometry (77±16 mmol/kg[8]) and skin density (1.1 kg/L[67]). While producing TSC estimates using simulated signal loss from *average* skin sodium relaxation measurement is interesting, it does not account for skin sodium relaxation differences between individuals, or (more importantly) potential change with pathology.

This study investigated ^{23}Na MRI in skin and confirmed with simulation that sodium image intensity loss and bias by skin thickness (which was shown to vary from 1 mm – 1.8 mm across individuals in this study) can be reduced with SNR-efficient surface coil imaging and high resolution 'pancake' voxel reshaping for small voxel dimensions across the skin. Simulation trends that matched experiments suggest that even TPI with TE ~ 0.1 ms is associated with considerable rapid biexponential relaxation related weighting. However, this weighting can be compensated if it is known. Future studies might consider imaging methodology that measures ^{23}Na relaxation for each individual to facilitate 'within-volunteer' correction for accurate TSC quantification.

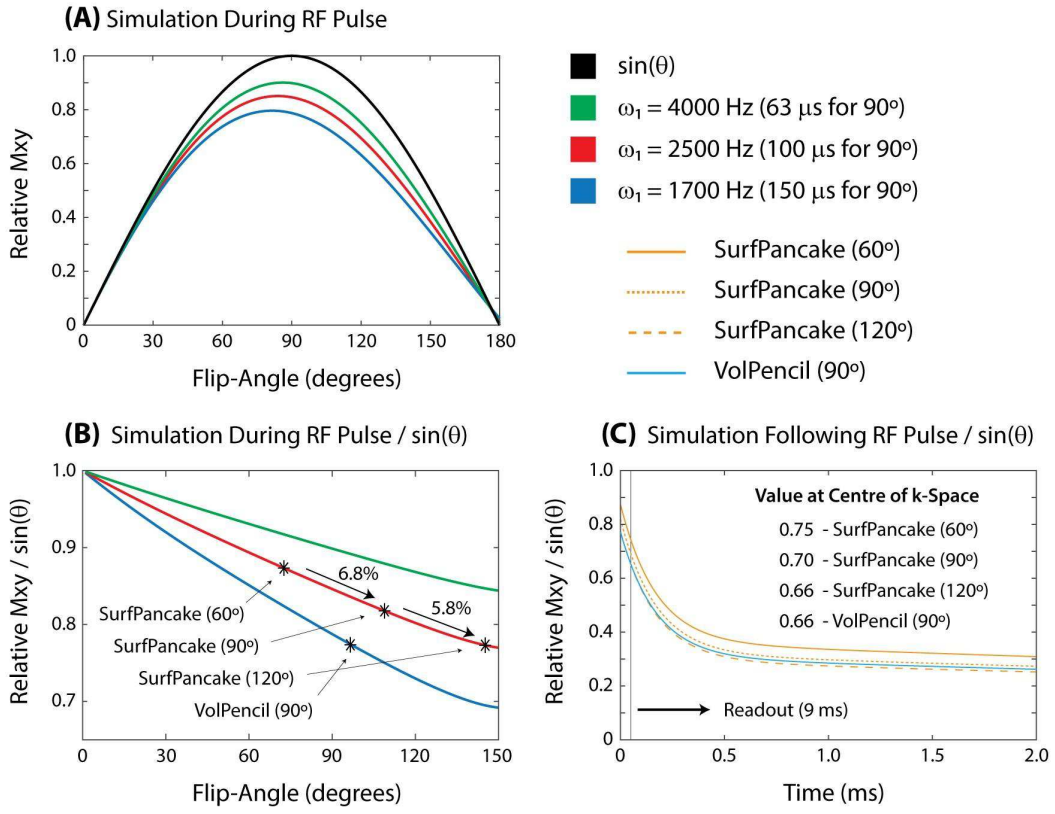

Figure 3.6: **(A)** The relative M_{xy} created during an excitation pulse is reduced from a dependence when skin relaxation with $T_{2fast(60\%)}$ = 0.17 ms and $T_{2slow(60\%)}$ = 12.5 ms[83] is included in simulation. The maximum signal is also shifted to lower flip-angles. This reduction and shift is greater for lower power RF pulses (i.e. lower ω_1). Note the ω_1 = 2500 Hz curve fits the skin B_1 analysis experiment of **Figure 2B**. **(B)** The normalized (by sin(θ)) M_{xy} decreases approximately linearly with a flip-angle over the range shown. The flip-angles achieved in skin with the *SurfPancake* protocol are plotted on this figure (note that flip-angles of 60°, 90°, and 120° were specified, and the average relative B_1 measured in skin was 1.21). Following B_1^+ correction (i.e. division by sin(θ)), simulation suggests a 6.8% signal decrease from *SurfPancake* (60°) to *SurfPancake* (90°), and a 5.8% signal decrease from *SurfPancake* (90°) to *SurfPancake* (120°). These values are very similar to the measured signal decrease between protocols given in **Figure 3B**. **(C)** Simulation following the RF pulse demonstrates that signal loss during the RF pulse is associated with approximately equal reduction of both the fast and slow decaying components of M_{xy}. Fitting the signal decay following excitation yields the same T_{2fast} and T_{2slow} as the simulation model (listed above), but slightly different T_{2fast} fractions of 58.5% for *SurfPancake* (60°), 60.8% for *SurfPancake* (90°), 61.8% for *SurfPancake* (120°), and 60.1% for *VolPencil* (90°). The relative M_{xy} values during the identified readout were used for subsequent simulated imaging.

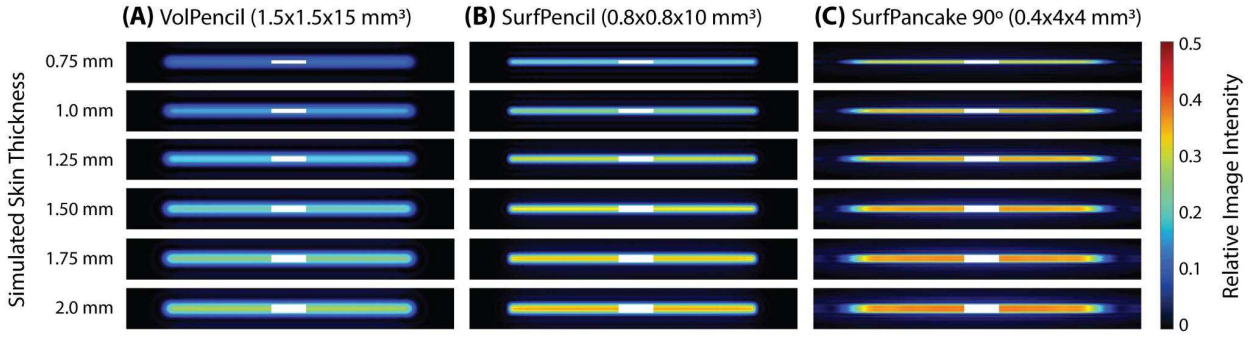

Figure 3.7: (A) Simulated images of skin were created by sampling k-space of *S*×60×60 mm^3 numerical boxes (with intensity = 1.0), where '*S*' is skin thickness ranging from 0.75 mm to 2.0 mm. k-Space values were then multiplied by the simulated relative M_{xy} over the duration of the readout, as depicted in **Figure 3.6C**. Simulated imaging yields progressively greater image intensity with skin thickness increase from 0.75 mm – 2.0 mm for the *VolPencil* voxels (1.5×1.5×15 mm^3). Note that on each plot, a white box is used to demarcate the simulated skin thickness (and only the skin thickness, not the width). Image intensity reduction from 1.0 (the true simulated skin signal value) is associated with both relative M_{xy} reduction at the centre of k-space (as identified in **Figure 3.6C**), and point spread function related smearing, which distributes the skin signal beyond the thickness of the skin. **(B)** The smaller *SurfPencil* voxels (0.8×0.8×10 mm^3) exhibit less signal smearing and greater relative intensity values within the skin. **(C)** The reshaped *SurfPancake* voxels with thickness of 0.4 mm across the skin yield even less signal smearing beyond the skin. Across skin thicknesses from 1.0 mm – 2.0 mm, the relative image intensity in the simulated skin appears quite consistent around the value of 0.35 (i.e. only ~ 1/3 of full value).

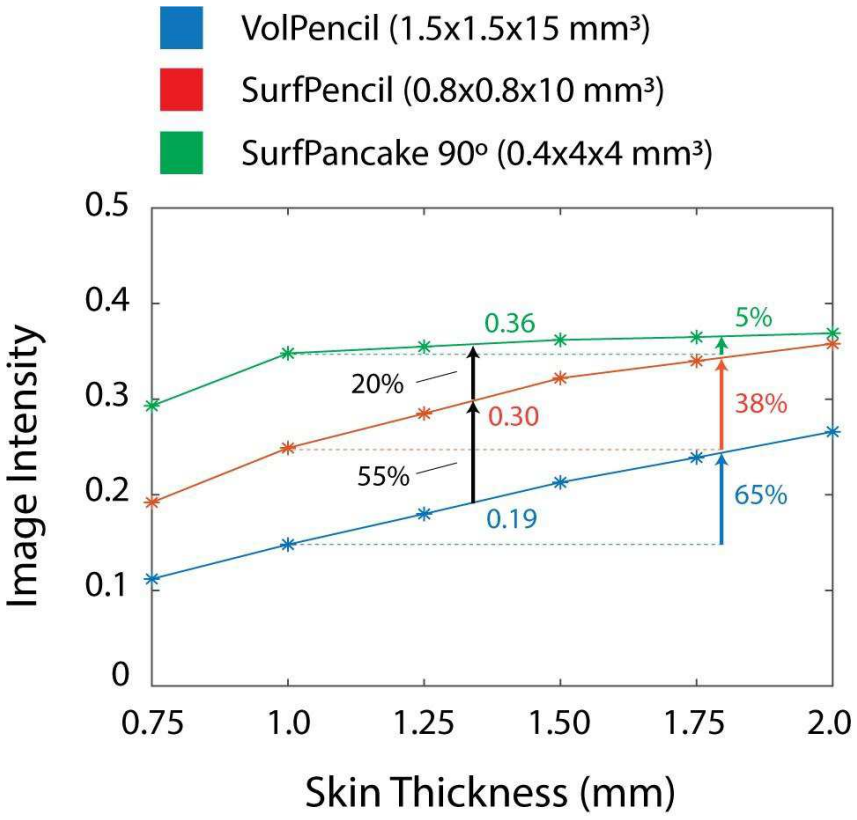

Figure 3.8: Simulated image intensities (from **Figure 3.7**) were measured in a (2 zero-filled voxel thick) ROI at the centre of skin (as for volunteer analysis), and are plotted here across skin thickness. Note that image intensity reduction from 1.0 represents signal loss with respect to M_o. At the average skin thickness of 1.34 mm (in this study), the *VolPencil*, *SurfPencil*, and *SurfPancake* (90°) protocols exhibit relative image intensities of only 0.19, 0.30, and 0.36, respectively. This amounts to a 55% image intensity increase for the *SurfPencil* protocol over the *VolPencil* protocol, and a further 20% increase for the *SurfPancake* (90°) protocol over *SurfPencil* (black arrows in figure). These increases are in the range of the average skin/agar increases in **Figure 3.3B**. Over the approximate skin thickness range in this paper (1.0 mm to 1.8 mm), image intensities of the *VolPencil*, *SurfPencil,* and *SurfPancake (90°)* protocols increase 65%, 38%, and 5%, respectively (coloured arrows). These increases are in the range of the regressed skin/agar increases from 1.0 mm to 1.8 mm listed for each protocol in **Figure 3.4**.

4 Conclusions

This study introduces significant advancements in the quantification of skin sodium concentrations through sodium MRI, improving upon the widely adopted volume coil protocol with low spatial resolution at 3×3×30 mm^3 and long TE at 2 ms. The proposed approach addresses limitations in the conventional methods by utilizing a combination of a twisted projection imaging (TPI) sequence and a surface coil, in contrast to the previously used volume coil and gradient echo (GRE) sequence. This method enhances signal capture by taking advantage of the short echo time (TE=0.1 ms), which is essential given the short biexponential T_2 relaxation times in skin (T_{2fast}=0.17 ms, T_{2slow}=12.5 ms[83]).

The application of a surface coil (along with smaller fully sampled FOV) allowed for the use of smaller voxel sizes, specifically reshaped to dimensions of 0.4×4×4=6.4 mm^3 (42× smaller voxel volume than Kopp protocol with similar scan time of ~ 12 minutes), significantly enhancing the signal-to-noise ratio (SNR) and improving skin tissue sodium concentration (TSC) measurement accuracy compared to the traditional volume coil protocol. The improved methodology which combined TPI, surface coil, flat 'pancake-shaped' voxels (*SurfPancake*) yielded skin TSC at 34 mM, this is higher than previous ~12-21 mM measured by the widely-adopted Kopp protocol, but still much lower than 85 mM expected from atomic absorption spectroscopy. Additionally, this study investigated the influence of skin thickness on TSC measurements, an important factor for bias that was not fully addressed in previous studies. Although the use of a short RF pulse duration reduced signal loss, there were still challenges in compensating for the sodium signal loss during RF excitation due to the very rapid biexpoential decay

in skin. PSF smearing also further contributes to signal loss. RF pulse length could be reduced by developing surface coil that can endure more RF power, or introducing smaller flip angles. Relaxation-based compensation was employed to recover a substantial amount of signal, yielded average TSC of 95 mM, which is similar to previous values obtained using atomic absorption spectroscopy (85 mM).

Despite these advancements, several limitations were encountered. The study's small sample size, particularly the limited number of older female volunteers, restricted our ability to assess variations in skin sodium concentrations across different ages and sexes. Furthermore, the agar phantoms used for calibration posed challenges due to mold growth and dehydration, which led to inconsistencies in sodium quantification. Future research could benefit from using sodium-free agar to allow for more controlled sodium concentration adjustments.

These findings suggest promising future research directions, including the development of RF coils capable of enduring shorter RF pulses and measuring individual relaxation parameters for signal compensation. This study lays the groundwork for more accurate and reliable skin sodium measurements, providing a foundation for future advancements skin TSC quantification.

In conclusion, the advancements proposed in this study present a significant leap forward in skin sodium quantification methods, offering enhanced accuracy and potential applications in clinical and research settings. Encouraging pilot data indicates that this improved methodology could be utilized in future studies to explore age-related changes,

sex differences, and a variety of clinical disorders where previous low-resolution protocols have implicated sodium abnormalities.

References

1. Jhee JH, Park HC, Choi HY. Skin Sodium and Blood Pressure Regulation. *Electrolytes Blood Press E BP*. 2022;20(1):1-9. doi:10.5049/EBP.2022.20.1.1

2. Burstein D, Springer Jr CS. Sodium MRI revisited. *Magn Reson Med*. 2019;82(2):521-524. doi:10.1002/mrm.27738

3. Siegel G, Walter A, Kauschmann A, Malmsten M, Buddecke E. Anionic biopolymers as blood flow sensors. *Biosens Bioelectron*. 1996;11(3):281-294. doi:10.1016/0956-5663(96)88415-6

4. Farber SJ, Schubert M, Schuster N. The binding of cations by chondroitin sulfate. *J Clin Invest*. 1957;36(12):1715-1722. doi:10.1172/JCI103573

5. Kopp C, Linz P, Dahlmann A, et al. 23Na magnetic resonance imaging-determined tissue sodium in healthy subjects and hypertensive patients. *Hypertension*. 2013;61(3):635-640. doi:10.1161/HYPERTENSIONAHA.111.00566

6. Dyke JP, Meyring-Wösten A, Zhao Y, Linz P, Thijssen S, Kotanko P. Reliability and agreement of sodium (23Na) MRI in calf muscle and skin of healthy subjects from the US. *Clin Imaging*. 2018;52:100-105. doi:10.1016/j.clinimag.2018.07.010

7. Linz P, Santoro D, Renz W, et al. Skin sodium measured with ^{23} Na MRI at 7.0 T. *NMR Biomed*. 2014;28:54-62. doi:10.1002/nbm.3224

8. Kopp C, Linz P, Wachsmuth L, et al. (23)Na magnetic resonance imaging of tissue sodium. *Hypertension*. 2012;59(1):167-172. doi:10.1161/HYPERTENSIONAHA.111.183517

9. Schneider MP, Raff U, Kopp C, et al. Skin Sodium Concentration Correlates with Left Ventricular Hypertrophy in CKD. *J Am Soc Nephrol*. 2017;28(6):1867-1876. doi:10.1681/ASN.2016060662

10. Rabelink TJ, Rotmans JI. Salt is getting under our skin. *Nephrol Dial Transplant*. 2009;24(11):3282-3283. doi:10.1093/ndt/gfp399

11. Kopp C, Beyer C, Linz P, et al. Na+ deposition in the fibrotic skin of systemic sclerosis patients detected by 23Na-magnetic resonance imaging. *Rheumatology*. 2017;56(4):556-560. doi:10.1093/rheumatology/kew371

12. Kopp C, Linz P, Maier C, et al. Elevated tissue sodium deposition in patients with type 2 diabetes on hemodialysis detected by 23Na magnetic resonance imaging.

Kidney Int. 2018;93(5):1191-1197. doi:10.1016/j.kint.2017.11.021

13. Selvarajah V, Connolly K, McEniery C, Wilkinson I. Skin Sodium and Hypertension: a Paradigm Shift? *Curr Hypertens Rep*. 2018;20(11):94. doi:10.1007/s11906-018-0892-9

14. Ellison D, Welling P. Insights into Salt Handling and Blood Pressure. *N Engl J Med*. 2021;385(21):1981-1993. doi:10.1056/NEJMra2030212

15. Wiig H, Luft FC, Titze JM. The interstitium conducts extrarenal storage of sodium and represents a third compartment essential for extracellular volume and blood pressure homeostasis. *Acta Physiol*. 2018;222(3):e13006. doi:10.1111/apha.13006

16. Sterns R. Disorders of Plasma Sodium — Causes, Consequences, and Correction. *N Engl J Med*. 2015;372(1):55-65. doi:10.1056/NEJMra1404489

17. EFSA Panel on Nutrition, Novel Foods and Food Allergens (NDA), Turck D, Castenmiller J, et al. Dietary reference values for sodium. *EFSA J*. 2019;17(9):e05778. doi:10.2903/j.efsa.2019.5778

18. Titze J, Lang R, Ilies C, et al. Osmotically inactive skin Na^+ storage in rats. *Am J Physiol-Ren Physiol*. 2003;285(6):F1108-F1117. doi:10.1152/ajprenal.00200.2003

19. Lyu Q, Gong S, Yin J, Dyson JM, Cheng W. Soft Wearable Healthcare Materials and Devices. *Adv Healthc Mater*. 2021;10(17):2100577. doi:10.1002/adhm.202100577

20. Madelin G, Regatte RR. Biomedical applications of sodium MRI in vivo. *J Magn Reson Imaging*. 2013;38(3):511-529. doi:10.1002/jmri.24168

21. Babsky AM, Hekmatyar SK, Zhang H, Solomon JL, Bansal N. Application of 23Na MRI to Monitor Chemotherapeutic Response in RIF-1 Tumors. *Neoplasia*. 2005;7(7):658-666. doi:10.1593/neo.05130

22. Zacchia M, Abategiovanni ML, Stratigis S, Capasso G. Potassium: From Physiology to Clinical Implications. *Kidney Dis*. 2016;2(2):72-79. doi:10.1159/000446268

23. Strazzullo P, Leclercq C. Sodium. *Adv Nutr Bethesda Md*. 2014;5:188-190. doi:10.3945/an.113.005215

24. Afsar B, Afsar RE. The role of glycosaminoglycans in blood pressure regulation. *Microcirculation*. 2023;30(8):e12832. doi:10.1111/micc.12832

25. Zhu H, Pollock NK, Kotak I, et al. Dietary Sodium, Adiposity, and Inflammation in Healthy Adolescents. *Pediatrics*. 2014;133(3):e635-e642. doi:10.1542/peds.2013-1794

26. Féraille E, Doucet A. Sodium-Potassium-Adenosinetriphosphatase-Dependent Sodium Transport in the Kidney: Hormonal Control. *Physiol Rev*. 2001;81(1):345-418. doi:10.1152/physrev.2001.81.1.345

27. Olde Engberink RHG, Selvarajah V, Vogt L. Clinical impact of tissue sodium storage. *Pediatr Nephrol Berl Ger*. 2020;35(8):1373-1380. doi:10.1007/s00467-019-04305-8

28. Hofmeister LH, Perisic S, Titze J. Tissue sodium storage: evidence for kidney-like extrarenal countercurrent systems? *Pflüg Arch - Eur J Physiol*. 2015;467(3):551-558. doi:10.1007/s00424-014-1685-x

29. Heer M, Baisch F, Kropp J, Gerzer R, Drummer C. High dietary sodium chloride consumption may not induce body fluid retention in humans. *Am J Physiol-Ren Physiol*. 2000;278(4):F585-F595. doi:10.1152/ajprenal.2000.278.4.F585

30. Titze J, Maillet A, Lang R, et al. Long-term sodium balance in humans in a terrestrial space station simulation study. *Am J Kidney Dis*. 2002;40(3):508-516. doi:10.1053/ajkd.2002.34908

31. Polychronopoulou E, Braconnier P, Burnier M. New Insights on the Role of Sodium in the Physiological Regulation of Blood Pressure and Development of Hypertension. *Front Cardiovasc Med*. 2019;6. doi:10.3389/fcvm.2019.00136

32. Titze J, Shakibaei M, Schafflhuber M, et al. Glycosaminoglycan polymerization may enable osmotically inactive Na+ storage in the skin. *Am J Physiol Heart Circ Physiol*. 2004;287(1):H203-208. doi:10.1152/ajpheart.01237.2003

33. Machnik A, Neuhofer W, Jantsch J, et al. Macrophages regulate salt-dependent volume and blood pressure by a vascular endothelial growth factor-C-dependent buffering mechanism. *Nat Med*. 2009;15(5):545-552. doi:10.1038/nm.1960

34. Xu W, Hong SJ, Zeitchek M, et al. Hydration Status Regulates Sodium Flux and Inflammatory Pathways through Epithelial Sodium Channel (ENaC) in the Skin. *J Invest Dermatol*. 2015;135(3):796-806. doi:10.1038/jid.2014.477

35. Agócs R, Sugár D, Pap D, Szabó A. [The immunomodulatory role of sodium]. *Orv Hetil*. 2019. doi:10.1556/650.2019.31292

36. Zhang MZ, Yao B, Wang Y, et al. Inhibition of cyclooxygenase-2 in hematopoietic cells results in salt-sensitive hypertension. *J Clin Invest*. 125(11):4281-4294. doi:10.1172/JCI81550

37. Pries AR, Secomb TW, Gaehtgens P. The endothelial surface layer. *Pflüg Arch*. 2000;440(5):653-666. doi:10.1007/s004240000307

38. Nieuwdorp M, Mooij HL, Kroon J, et al. Endothelial Glycocalyx Damage Coincides With Microalbuminuria in Type 1 Diabetes. *Diabetes*. 2006;55(4):1127-1132. doi:10.2337/diabetes.55.04.06.db05-1619

39. Pohl HR, Wheeler JS, Murray HE. Sodium and Potassium in Health and Disease. In: Sigel A, Sigel H, Sigel RKO, eds. *Interrelations between Essential Metal Ions and Human Diseases*. Dordrecht: Springer Netherlands; 2013:29-47. doi:10.1007/978-94-007-7500-8_2

40. Lemoine S, Salerno FR, Akbari A, McKelvie RS, McIntyre CW. Tissue Sodium Storage in Patients With Heart Failure: A New Therapeutic Target? *Circ Cardiovasc Imaging*. 2021;14(11):e012910. doi:10.1161/CIRCIMAGING.121.012910

41. Jantsch J, Schatz V, Friedrich D, et al. Cutaneous Na+ Storage Strengthens the Antimicrobial Barrier Function of the Skin and Boosts Macrophage-Driven Host Defense. *Cell Metab*. 2015;21(3):493-501. doi:10.1016/j.cmet.2015.02.003

42. Crescenzi R, Marton A, Donahue PMC, et al. Tissue Sodium Content is Elevated in the Skin and Subcutaneous Adipose Tissue in Women with Lipedema. *Obesity*. 2018;26(2):310-317. doi:10.1002/oby.22090

43. Crescenzi R, Donahue PMC, Petersen KJ, et al. Upper and Lower Extremity Measurement of Tissue Sodium and Fat Content in Patients with Lipedema. *Obesity*. 2020;28(5):907-915. doi:10.1002/oby.22778

44. Donahue PMC, Crescenzi R, Petersen KJ, et al. Physical Therapy in Women with Early Stage Lipedema: Potential Impact of Multimodal Manual Therapy, Compression, Exercise, and Education Interventions. *Lymphat Res Biol*. 2022;20(4):382-390. doi:10.1089/lrb.2021.0039

45. Maifeld A, Wild J, Karlsen TV, et al. Skin Sodium Accumulates in Psoriasis and Reflects Disease Severity. *J Invest Dermatol*. 2022;142(1):166-178.e8. doi:10.1016/j.jid.2021.06.013

46. Ott C, Kopp C, Dahlmann A, et al. Impact of renal denervation on tissue Na+ content in treatment-resistant hypertension. *Clin Res Cardiol Off J Ger Card Soc*. 2018;107(1):42-48. doi:10.1007/s00392-017-1156-4

47. Alsouqi A, Deger SM, Sahinoz M, et al. Tissue Sodium in Patients With Early Stage Hypertension: A Randomized Controlled Trial. *J Am Heart Assoc*. 2022;11(8):e022723. doi:10.1161/JAHA.121.022723

48. Hammon M, Grossmann S, Linz P, et al. 23Na Magnetic Resonance Imaging of the Lower Leg of Acute Heart Failure Patients during Diuretic Treatment. *PLOS ONE*.

2015;10(10):e0141336. doi:10.1371/journal.pone.0141336

49. Kannenkeril D, Karg MV, Bosch A, et al. Tissue sodium content in patients with type 2 diabetes mellitus. *J Diabetes Complications*. 2019;33(7):485-489. doi:10.1016/j.jdiacomp.2019.04.006

50. Karg MV, Bosch A, Kannenkeril D, et al. SGLT-2-inhibition with dapagliflozin reduces tissue sodium content: a randomised controlled trial. *Cardiovasc Diabetol*. 2018;17(1):5. doi:10.1186/s12933-017-0654-z

51. Christa M, Weng AM, Geier B, et al. Increased myocardial sodium signal intensity in Conn's syndrome detected by 23Na magnetic resonance imaging. *Eur Heart J - Cardiovasc Imaging*. 2019;20(3):263-270. doi:10.1093/ehjci/jey134

52. Carranza-León DA, Oeser A, Marton A, et al. Tissue sodium content in patients with systemic lupus erythematosus: association with disease activity and markers of inflammation. *Lupus*. 2020;29(5):455-462. doi:10.1177/0961203320908934

53. Chifu I, Weng AM, Burger-Stritt S, et al. Non-invasive assessment of tissue sodium content in patients with primary adrenal insufficiency. *Eur J Endocrinol*. 2022;187(3):383-390. doi:10.1530/EJE-22-0396

54. Huhn K, Linz P, Pemsel F, et al. Skin sodium is increased in male patients with multiple sclerosis and related animal models. *Proc Natl Acad Sci U S A*. 2021;118(28):e2102549118. doi:10.1073/pnas.2102549118

55. Qirjazi E, Salerno FR, Akbari A, et al. Tissue sodium concentrations in chronic kidney disease and dialysis patients by lower leg sodium-23 magnetic resonance imaging. *Nephrol Dial Transplant*. 2021;36(7):1234-1243. doi:10.1093/ndt/gfaa036

56. Salerno FR, Akbari A, Lemoine S, Scholl TJ, McIntyre CW, Filler G. Effects of pediatric chronic kidney disease and its etiology on tissue sodium concentration: a pilot study. *Pediatr Nephrol*. 2023;38(2):499-507. doi:10.1007/s00467-022-05600-7

57. Hammon M, Grossmann S, Linz P, et al. 3 Tesla 23Na Magnetic Resonance Imaging During Acute Kidney Injury. *Acad Radiol*. 2017;24(9):1086-1093. doi:10.1016/j.acra.2017.03.012

58. Friedrich AC, Linz P, Nagel AM, et al. Hemodialysis Patients with Cardiovascular Disease Reveal Increased Tissue Na+ Deposition. *Kidney Blood Press Res*. 2021;47(3):185-193. doi:10.1159/000520821

59. Dahlmann A, Dörfelt K, Eicher F, et al. Magnetic resonance-determined sodium removal from tissue stores in hemodialysis patients. *Kidney Int*. 2015;87(2):434-441.

doi:10.1038/ki.2014.269

60. Sahinoz M, Tintara S, Deger SM, et al. Tissue sodium stores in peritoneal dialysis and hemodialysis patients determined by sodium-23 magnetic resonance imaging. *Nephrol Dial Transplant*. 2021;36(7):1307-1317. doi:10.1093/ndt/gfaa350

61. Salerno FR, Akbari A, Lemoine S, Filler G, Scholl TJ, McIntyre CW. Outcomes and predictors of skin sodium concentration in dialysis patients. *Clin Kidney J*. 2022;15(6):1129-1136. doi:10.1093/ckj/sfac021

62. Matthias J, Maul J, Noster R, et al. Sodium chloride is an ionic checkpoint for human TH2 cells and shapes the atopic skin microenvironment. *Sci Transl Med*. 2019;11(480):eaau0683. doi:10.1126/scitranslmed.aau0683

63. Chen JY, Chew KS, Mary S, et al. Skin-specific mechanisms of body fluid regulation in hypertension. *Clin Sci*. 2023;137(3):239-250. doi:10.1042/CS20220609

64. Abdel Ghafar MT. An overview of the classical and tissue-derived renin-angiotensin-aldosterone system and its genetic polymorphisms in essential hypertension. *Steroids*. 2020;163:108701. doi:10.1016/j.steroids.2020.108701

65. Chen L, He FJ, Dong Y, Huang Y, Harshfield GA, Zhu H. Sodium Reduction, miRNA Profiling and CVD Risk in Untreated Hypertensives: a Randomized, Double-Blind, Placebo-Controlled Trial. *Sci Rep*. 2018;8(1):12729. doi:10.1038/s41598-018-31139-5

66. Fischereder M, Michalke B, Schmöckel E, et al. Sodium storage in human tissues is mediated by glycosaminoglycan expression. *APSselect*. 2017;4(6):F319-F325. doi:10.1152/ajprenal.00703.2016@apsselect.2017.4.issue-6

67. Gennisson JL, Baldeweck T, Tanter M, et al. Assessment of elastic parameters of human skin using dynamic elastography. *IEEE Trans Ultrason Ferroelectr Freq Control*. 2004;51(8):980-989. doi:10.1109/TUFFC.2004.1324402

68. Giacomoni PU, Mammone T, Teri M. Gender-linked differences in human skin. *J Dermatol Sci*. 2009;55(3):144-149. doi:10.1016/j.jdermsci.2009.06.001

69. Wang S, Yu RX, Fan W, et al. Detection of skin thickness and density in healthy Chinese people by using high-frequency ultrasound. *Skin Res Technol*. 2023;29(1):e13219. doi:10.1111/srt.13219

70. Dąbrowska M, Mielcarek A, Nowak I. Evaluation of sex-related changes in skin topography and structure using innovative skin testing equipment. *Skin Res Technol*. 2018;24(4):614-620. doi:10.1111/srt.12473

71. Lasagni C, Seidenari S. Echographic assessment of age-dependent variations of skin thickness. *Skin Res Technol*. 1995;1(2):81-85. doi:10.1111/j.1600-0846.1995.tb00022.x

72. Shuster S, Black MM, McVitie E. The influence of age and sex on skin thickness, skin collagen and density. *Br J Dermatol*. 1975;93(6):639-643. doi:10.1111/j.1365-2133.1975.tb05113.x

73. Branchet MC, Boisnic S, Frances C, Robert AM. Skin Thickness Changes in Normal Aging Skin. *Gerontology*. 2009;36(1):28-35. doi:10.1159/000213172

74. Quan T, Fisher GJ. Role of Age-Associated Alterations of the Dermal Extracellular Matrix Microenvironment in Human Skin Aging: A Mini-Review. *Gerontology*. 2015;61(5):427-434. doi:10.1159/000371708

75. Lee Y, Hwang K. Skin thickness of Korean adults. *Surg Radiol Anat*. 2002;24(1):183-189. doi:https://doi.org/10.1007/s00276-002-0034-5

76. Seidenari S, Giusti G, Bertoni L, Magnoni C, Pellacani G. Thickness and Echogenicity of the Skin in Children as Assessed by 20-MHz Ultrasound. *Dermatol Basel Switz*. 2000;201:218-222. doi:10.1159/000018491

77. Deger SM, Wang P, Fissell R, et al. Tissue sodium accumulation and peripheral insulin sensitivity in maintenance hemodialysis patients. *J Cachexia Sarcopenia Muscle*. 2017;8(3):500-507. doi:10.1002/jcsm.12179

78. Rooney WD, Springer CS. The molecular environment of intracellular sodium: 23Na NMR relaxation. *NMR Biomed*. 1991;4(5):227-245. doi:10.1002/nbm.1940040503

79. Pekar J, Renshaw PF, Leigh JS. Selective detection of intracellular sodium by coherence-transfer NMR. *J Magn Reson*. 1987;72(1):159-161. doi:10.1016/0022-2364(87)90182-X

80. Van Der Maarel JRC. Relaxation of spin 32 in a nonzero average electric field gradient. *Chem Phys Lett*. 1989;155(3):288-296. doi:10.1016/0009-2614(89)85327-8

81. Madelin G, Jerschow A, Regatte RR. Sodium relaxation times in the knee joint in vivo at 7T. *Nmr Biomed*. 2012;25(4):530-537. doi:10.1002/nbm.1768

82. Coste A, Boumezbeur F, Vignaud A, et al. Tissue sodium concentration and sodium T1 mapping of the human brain at 3 T using a Variable Flip Angle method. *Magn Reson Imaging*. 2019;58:116-124. doi:10.1016/j.mri.2019.01.015

83. Stobbe R, Zhu J, Beaulieu C. Flip-Angle and Signal Dependence on RF Pulse Duration Yield Measurement of Very Rapid T2f for (23)Na in Skin. Presented at:

ISMRM Workshop on MR Imaging of X-Nuclei ((23)Na & Friends); 2023;Marseille, France.

84. Worthoff WA, Shymanskaya A, Shah NJ. Relaxometry and quantification in simultaneously acquired single and triple quantum filtered sodium MRI. *Magn Reson Med*. 2019;81(1):303-315. doi:10.1002/mrm.27387

85. Feldman RE, Stobbe R, Watts A, Beaulieu C. Sodium imaging of the human knee using soft inversion recovery fluid attenuation. *J Magn Reson*. 2013;234:197-206. doi:10.1016/j.jmr.2013.06.021

86. Kordzadeh A, Duchscherer J, Beaulieu C, Stobbe R. Radiofrequency excitation–related 23Na MRI signal loss in skeletal muscle, cartilage, and skin. *Magn Reson Med*. 2020;83(6):1992-2001. doi:10.1002/mrm.28054

87. Ouwerkerk R. Sodium MRI. In: Modo M, Bulte JWM, eds. *Magnetic Resonance Neuroimaging: Methods and Protocols*. Totowa, NJ: Humana Press; 2011:175-201. doi:10.1007/978-1-61737-992-5_8

88. Nielles-Vallespin S, Weber MA, Bock M, et al. 3D radial projection technique with ultrashort echo times for sodium MRI: Clinical applications in human brain and skeletal muscle. *Magn Reson Med*. 2007;57(1):74-81. doi:10.1002/mrm.21104

89. Nagel AM, Laun FB, Weber MA, Matthies C, Semmler W, Schad LR. Sodium MRI using a density-adapted 3D radial acquisition technique. *Magn Reson Med*. 2009;62(6):1565-1573. doi:10.1002/mrm.22157

90. Willmering MM, Robison RK, Wang H, Pipe JG, Woods JC. Implementation of the FLORET Ultrashort Echo-Time Sequence for Lung Imaging. *Magn Reson Med*. 2019;82(3):1091-1100. doi:10.1002/mrm.27800

91. Boada FE, Gillen JS, Shen GX, Chang SY, Thulborn KR. Fast three dimensional sodium imaging. *Magn Reson Med*. 1997;37(5):706-715. doi:10.1002/mrm.1910370512

92. Gurney PT, Hargreaves BA, Nishimura DG. Design and analysis of a practical 3D cones trajectory. *Magn Reson Med*. 2006;55(3):575-582. doi:10.1002/mrm.20796

93. Romanzetti S, Mirkes CC, Fiege DP, Celik A, Felder J, Shah NJ. Mapping tissue sodium concentration in the human brain: A comparison of MR sequences at 9.4 Tesla. *NeuroImage*. 2014;96:44-53. doi:10.1016/j.neuroimage.2014.03.079

94. Lu A, Atkinson IC, Claiborne TC, Damen FC, Thulborn KR. Quantitative Sodium Imaging with a Flexible Twisted Projection Pulse Sequence. *Magn Reson Med*.

2010;63(6):1583-1593. doi:10.1002/mrm.22381

95. Jin J. *Electromagnetic Analysis and Design in Magnetic Resonance Imaging*. New York: Routledge; 2017. doi:10.1201/9780203758731

96. Gruber B, Froeling M, Leiner T, Klomp DWJ. RF coils: A practical guide for nonphysicists. *J Magn Reson Imaging*. 2018;48(3):590-604. doi:10.1002/jmri.26187

97. Giovannetti G, Flori A, Martini N, et al. Sodium Radiofrequency Coils for Magnetic Resonance: From Design to Applications. *Electronics*. 2021;10(15):1788. doi:10.3390/electronics10151788

98. Giovannetti G, Pingitore A, Positano V, et al. Improving sodium Magnetic Resonance in humans by design of a dedicated 23Na surface coil. *Measurement*. 2014;50:285-292. doi:10.1016/j.measurement.2014.01.006

99. Milani B, Delacoste J, Burnier M, Pruijm M. Exploring a new method for quantitative sodium MRI in the human upper leg with a surface coil and symmetrically arranged reference phantoms. *Quant Imaging Med Surg*. 2019;9(6):985. doi:10.21037/qims.2019.06.08

100. Sacolick LI, Wiesinger F, Hancu I, Vogel MW. B1 mapping by Bloch-Siegert shift. *Magn Reson Med*. 2010;63(5):1315-1322. doi:10.1002/mrm.22357

101. Nöth U, Shrestha M, Deichmann R. B1 mapping using an EPI-based double angle approach: A practical guide for correcting slice profile and B0 distortion effects. *Magn Reson Med*. 2023;90(1):103-116. doi:10.1002/mrm.29632

102. Allen SP, Morrell GR, Peterson B, et al. Phase-sensitive sodium B1 mapping. *Magn Reson Med*. 2011;65(4):1125-1130. doi:10.1002/mrm.22700

103. Lommen J, Konstandin S, Krämer P, Schad LR. Enhancing the quantification of tissue sodium content by MRI: time-efficient sodium B1 mapping at clinical field strengths. *NMR Biomed*. 2016;29(2):129-136. doi:10.1002/nbm.3292

104. Vaeggemose M, Schulte RF, Laustsen C. Clinically feasible B1 field correction for multi-organ sodium imaging at 3 T. *NMR Biomed*. 2023;36(2):e4835. doi:10.1002/nbm.4835

105. Nagel A, Lehmann-Horn F, Weber A, et al. In Vivo 35 Cl MR Imaging in Humans: A Feasibility Study. *Radiology*. 2014;271:131725. doi:10.1148/radiol.13131725

106. Markó L, Dörr A, Linz P, et al. Effect of Sunitinib Treatment on Skin Sodium Accumulation in Patients With Renal Cancer: a Pilot Study. *Hypertension*. 2022;79(5):e103-e105. doi:10.1161/HYPERTENSIONAHA.122.19079

107. Oh JH, Kim YK, Jung JY, et al. Intrinsic aging- and photoaging-dependent level changes of glycosaminoglycans and their correlation with water content in human skin. *J Dermatol Sci*. 2011;62(3):192-201. doi:10.1016/j.jdermsci.2011.02.007

108. Firooz A, Rajabi-Estarabadi A, Zartab H, Pazhohi N, Fanian F, Janani L. The influence of gender and age on the thickness and echo-density of skin. *Skin Res Technol*. 2017;23(1):13-20. doi:10.1111/srt.12294

109. Bağcı IS, Ruini C, Niesert AC, et al. Effects of Short-Term Moisturizer Application in Different Ethnic Skin Types: Noninvasive Assessment with Optical Coherence Tomography and Reflectance Confocal Microscopy. *Skin Pharmacol Physiol*. 2018;31(3):125-133. doi:10.1159/000486626

110. Sheppard RH. Skin Thickness in Endocrine Disease: A Roentgenographic Study. *Ann Intern Med*. 1967;66(3):531. doi:10.7326/0003-4819-66-3-531

111. Rodnan GP, Lipinski E, Luksick J. Skin thickness and collagen content in progressive systemic sclerosis and localized scleroderma. *Arthritis Rheum*. 1979;22(2):130-140. doi:10.1002/art.1780220205

112. Hayes CE, Axel L. Noise performance of surface coils for magnetic resonance imaging at 1.5 T. *Med Phys*. 1985;12(5):604-607. doi:10.1118/1.595682

113. Rooney WD, Springer Jr CS. A comprehensive approach to the analysis and interpretation of the resonances of spins 3/2 from living systems. *NMR Biomed*. 1991;4(5):209-226. doi:10.1002/nbm.1940040502

114. Hancu I, Maarel J, Boada F. A Model for the Dynamics of Spins 3/2 in Biological Media: Signal Loss during Radiofrequency Excitation in Triple-Quantum-Filtered Sodium MRI. *J Magn Reson*. 2000;147(2):179-191. doi:10.1006/jmre.2000.2177.

115. Romanzetti S, Halse M, Kaffanke J, Zilles K, Balcom BJ, Shah NJ. A comparison of three SPRITE techniques for the quantitative 3D imaging of the 23Na spin density on a 4T whole-body machine. *J Magn Reson San Diego Calif 1997*. 2006;179(1):64-72. doi:10.1016/j.jmr.2005.11.007

116. Stobbe RW, Beaulieu C. Calculating potential error in sodium MRI with respect to the analysis of small objects. *Magn Reson Med*. 2018;79(6):2968-2977. doi:10.1002/mrm.26962

117. Blunck Y, Moffat BA, Kolbe SC, Ordidge RJ, Cleary JO, Johnston LA. Zero-gradient-excitation ramped hybrid encoding (zGRF -RHE) sodium MRI. *Magn Reson Med*. 2019;81(2):1172-1180. doi:10.1002/mrm.27484

118. Chao CYL, Zheng YP, Cheing GLY. The Association Between Skin Blood Flow and Edema on Epidermal Thickness in the Diabetic Foot. *Diabetes Technol Ther*. 2012;14(7):602-609. doi:10.1089/dia.2011.0301

119. Banba A, Koshiyama M, Watanabe Y, et al. Measurement of Skin Thickness Using Ultrasonography to Test the Usefulness of Elastic Compression Stockings for Leg Edema in Pregnant Women. *Healthcare*. 2022;10(9):1754. doi:10.3390/healthcare10091754

120. Davydov DA, Budylin GS, Baev AV, et al. Monitoring the skin structure during edema in vivo with spatially resolved diffuse reflectance spectroscopy. *J Biomed Opt*. 2023;28(05). doi:10.1117/1.JBO.28.5.057002